Chapter 12
Reduced Order Heat Exchanger Models for Low-to-Medium Temperature Range Solar Thermal Applications

Rudrodip Majumdar and Sandip K. Saha

Abstract Pivotal heat transfer components of solar thermal systems may involve single phase flow of the working fluid in some unit (e.g. single phase solar collector), whereas, two phase flow of the working fluid occurs in the other units (e.g. two-phase solar collector coupled directly to the turbine, boilers and evaporators). Modelling of these systems are important to understand the heat transfer behavior, as well as, to develop the system level control among many other attributes. A detailed analysis of single phase and two phase systems is possible using mathematical models to characterize the fluid flow and heat transfer. Detailed description of the fluid flow and heat transfer become computationally very expensive with such models, and also a very high level of precision may not be required in large time (∼few hours) simulations of the systems, as well as, in controlling the entire solar thermal power plant. Hence there is a need to develop computationally fast, low order dynamic models. Among many other modelling approaches, a particular class of heat exchanger model, namely the moving boundary lumped-parameter model, has emerged as an efficient and effective tool for simulating dynamic characteristics of the two-phase solar collectors and the evaporators, pertinent to organic Rankine cycle (ORC) systems. These models are efficient in locating the continuously moving working fluid phase change boundary without requiring any sophisticated, well-trained formulation pertinent to the starting solutions. Even a simplified, reduced order quasi-steady state model is capable of demonstrating moving boundary characteristics in a narrow evaporator tube that is employed to carry organic refrigerant (working fluid) into the two-phase ORC heat exchanger in the medium temperature solar thermal applications (∼200 °C). The model is capable of predicting the variation in working fluid mass flow rates with time-varying temperature of the heat transfer fluid (usually a

---

R. Majumdar (✉)
Department of Energy Science and Engineering, Indian Institute of Technology Bombay, Mumbai, India
e-mail: rudro.associates@gmail.com

S. K. Saha
Department of Mechanical Engineering, Indian Institute of Technology Bombay, Mumbai, India

H. Tyagi et al. (eds.), *Advances in Solar Energy Research*, Energy, Environment, and Sustainability, https://doi.org/10.1007/978-981-13-3302-6_12

commercial thermic oil), that transfers energy into the organic refrigerant. The variation in wall temperatures of the evaporator tube for three distinct flow regimes of the working fluid (subcooled, two-phase and superheated) can be evaluated with changing average heat transfer fluid (HTF) temperature, corresponding to the varying levels of solar radiation incident on the collectors; and therefore, the model provides an avenue for ascertaining the practicability of the operating conditions based on the variation of the driving parameters values. By using the results of the quasi-steady model as the initial guess in the detailed dynamic model, the sharp transient characteristics can be explored by introducing time-dependent fluctuations in the subcooled refrigerant flow at the heat exchanger entry. Further complexity can be added to the modelling by incorporating axial variation in the heat transfer fluid temperature profile in the prevalent shell and tube heat exchanger. In this monograph, we will briefly discuss about the full-fledged numerical models followed by elaborate description on reduced order models.

Keywords Reduced order modelling · Solar thermal system · Moving boundary model

Nomenclature

A	Area of cross section (m^2)
c	Specific heat (J/kg K)
D	Diameter of tube (m)
h	Specific enthalpy (J/kg)
$\bar{h}$	Average specific enthalpy (J/kg)
k	Thermal conductivity (W/m K)
L	Length (m)
$\dot{m}$	Mass flow rate (kg/s)
p	Pressure (Pa or bar)
p_o	Steady state mean pressure (Pa or bar)
$\tilde{P}$	Solar Irradiation (W/m^2)
q''	Heat flux (W/m^2)
T	Temperature (K or °C)
$\widetilde{T}$	Average temperature (K or °C)
t	Time (s or min)
u	Internal energy (J/kg)
v	Velocity (m/s)
z	Distance along length (m)

Greek Symbols

α	Heat transfer coefficient (W/m^2 K)
δ	Thermal boundary layer thickness in the thermic oil side (m)
η	Efficiency

ρ	Density (kg/m^3)
$\bar{\rho}$	Average density (kg/m^3)

Subscripts

1	Subcooled region
2	Two-phase region
3	Superheated region
12	Interface 1-2
23	Interface 2-3
b	Boiler
f	Saturated liquid
conv	Convective
g	Saturated gas
l	Liquid
HTF	Heat transfer fluid
HE	Heat Exchanger
i	Inner side of the tube
in	Inlet of tube or tank
o	Outer side of the tube
out	Outlet of tube or tank
lower	Lower end of the limit
Rfg	Refrigerant
sat	Saturation
Solar	Solar
sub	Subcooled
turbine	Turbine
upper	Upper end of the limit
wall	Wall

Abbreviation

DHW	Domestic hot water
HE	Heat exchanger
HTF	Heat transfer fluid
NIST	National Institute of Standards and Technology
ORC	Organic Rankine cycle
PPS	Peak to peak swing
TPHE	Two phase heat exchanger

12.1 Introduction

Earth receives more energy from the sun in just one hour than what the world consumes collectively over a period of one year (Thirugnanasambandam et al. 2010). India, in particular, receives average annual solar radiation amounting to over 5×10^{15} kWh (MNRE Annual Report 2006), with the average diurnal incident energy varying between 4 and 7 kWh/m^2 depending on the location (Mani and Rangarajan 1982). Therefore, harnessing of the solar energy potential is of interest in order to address the ever increasing demand for the usable energy. Studies indicate that the largest utility expense for a household is the cost to make hot water. Typically, on an average about 20% of total energy consumption in a household is attributed to the domestic hot water applications (e.g. cooking, cleaning, bathing) and the share increases to about 50% if the hot water is also used for heating purposes (Solar Thermal Hot Water Systems and Individual Components 2018). Naturally solar thermal energy technologies in particular have emerged as lucrative options for the domestic hot water (DHW) systems as well as for the production of heat for residential space heating (Thirugnanasambandam et al. 2010; Solar Thermal Hot Water Systems and Individual Components 2018; Kalogirou and Tripanagnostopoulos 2006; Natural Resources Canada 2005; Pinel et al. 2011; Weiss 2012; Evarts and Swan 2013; Aguilar et al. 2005; Fairey and Parker 2004; Becker and Stogsdill 1990; Mills 2004; Mathioulakis and Belessiotis 2002; Davidson 2005; Sarbu and Adam 2011; Baddou 2017; Homola 2018; Renewable Energy Solutions 2018). The earliest commercial solar water heater was introduced by Clarence Kemp in the 1890s in California. This primitive heating system was a simple batch type solar water heater that combined the collector and the storage in a single box. For an investment of $25, the annual savings in the coal costs was found to be about $9 (Homola 2018). The variation in the expenses incurred depends on the size of a system, amount of the water to be heated, the type of fuel used to heat water and how the heating system fits into the existing plumbing. Generally, the solar hot water systems designed for the warmer places (e.g. thermosiphon systems) are cheaper and more efficient compared to the more complex systems used in the colder regions (e.g. systems with vacuum tube collectors, pumps, heat exchangers, antifreeze mixtures, controls). Typically, the solar domestic hot water systems in Europe are sized to provide approximately 50–70% of the annual heating load (Renewable Energy Solutions 2018).

Design of low-to-medium temperature solar thermal systems needs to consider the heat transfer fundamentals in connection with the solar radiation levels, the collector configurations, the transfer of the collected heat and the storage of the collected heat to ensure reliable long-term system performance (Lunde 1980). Solar water heating systems use heat exchangers to transfer solar energy absorbed in solar collectors to the heat transfer fluid (liquid or air) used to heat water or a space. Heat exchangers (HE) are usually made of metals with reasonably high thermal conductivity, e.g. steel, copper, bronze, stainless steel, aluminium, cast iron etc. For the domestic solar heating systems copper is prevalently used in HE, due to its high thermal conductivity (~386 W/m K at 20 °C) as well as higher resistance to corrosion compared to the other candidates (Heat Exchangers for Solar Water Heating Systems 2018). The simplest form of heat transfer is single-phase heat exchange, where the heat transfer fluid (HTF) remains in the same phase (i.e. liquid or gas) throughout the process. The plate heat exchangers are the most studied and prevalently used heat exchanger configuration for the single phase liquid to liquid or air to liquid heat transfer (Nilpueng and Wongwises 2015; Khan et al. 2010; Li and Hrnjak 2016; Kim and Park 2017; Muley and Manglik 1997).

In a single-phase heat exchanger (SPHE), usually a liquid is preferred over the gas for the heat transfer process, since a liquid is a better thermal conductor than a gas, and therefore it requires much less surface area for effective heat transfer. The amount of heat transfer from one fluid to another is directly proportional to the temperature difference between the fluids. By keeping the heat load unchanged, the temperature difference between the working fluids can be increased either by raising the temperature of the heat source fluid, and/or by lowering the temperature of the heat sink fluid. The temperature difference can also be enhanced by increasing the mass flow rate of one (or, ideally both) of the fluids (Single Phase Fluid Coils 2018; Mehendale 2017). Although, it is to be mentioned that in case of unchanged heat load, a large temperature difference or higher flow rate will cause reduction in heat transfer time.

An alternative way of single phase heating employs 'thermosyphon', where passive heat exchange takes place due to the natural convection that circulates the liquid (working fluid) without the necessity of a mechanical pump (Kalogirou 2009; Koffi et al. 2008; Hobson and Norton 1988; Tang et al. 2010; Zelzouli et al. 2014; Tchuen and Koholé 2017; Taherian et al. 2011). Several experimental as well as numerical studies pertinent to the thermosyphon systems in connection with flat plate solar collectors have been previously reported along with some performance metrics (Koffi et al. 2008; Hobson and Norton 1988; Tang et al. 2010; Zelzouli et al. 2014; Tchuen and Koholé 2017; Taherian et al. 2011). One of the key performance parameter is the energy efficiency of the solar collector, which is expressed as the ratio of the amount of useful heat collected to the total amount of solar radiation striking the collector surface during any period of time (Tchuen and Koholé 2017). The energy efficiency of the thermosyphon solar water heating (TSWH) systems with different flat-plate collector configurations (based on the position of the riser tubes) have been previously reported for the same weather conditions. For the absorber-pipe lower bond configuration (i.e. riser tubes are welded above the absorber tube), the average value of the energy efficiency was found to be about 39.47%. The reported value of energy efficiency for the absorber-pipe side bond configuration (i.e. the absorber tube is welded in a way such that each interior absorber tube segment connects two consecutive riser tubes in the array) is 34.86% and that for the absorber-pipe upper bond configuration (i.e. the riser tuber welded below the absorber tube) is 32.28% (Tchuen and Koholé 2017).

For plant-scale production of solar thermal energy (in the range of hundreds of $\mathrm{kW_t}$ to $\mathrm{MW_t}$) the heat exchangers are configured to work in the two-phase flow mode where latent heat of evaporation of a vapour-liquid mixture is used to improve the transport capacity as well as to enhance the heat transfer process

(Kakaç et al. 1988; Shoureshi and McLaughlin 1984; Manglik 2006; Thome 1990). Simulation of the dynamic response of two-phase heat exchangers (TPHE) is of interest in order to increase reliability of various thermofluid systems as well as to facilitate significant energy savings (Shoureshi and McLaughlin 1984). Several computer codes have been previously developed to analyze the design and operational characteristics of residential heating and cooling equipment. Significant effort has been put towards the derivation of accurate, simple dynamic models of heat exchangers (Shoureshi and McLaughlin 1984; Paynter and Takahashi 1956; Wormley and Masada 1982; Pingaud et al. 1989; Roetzel 1996; Du et al. 1996; Roetzel and Xuan 1999).

Available literature has reported very few analytical solutions pertinent to heat flow and diffusion processes that involve phase change of the working fluid in a solar thermal system in particular and in similar relevant physical systems in general (Mongibello et al. 2014; Endalew and Abebe 2012). In connection to the solar thermal applications, a few implicit as well as mixed numerical techniques can be found in the published literatures, accompanied by different solution approaches and assumptions. Transient numerical model for the solar domestic hot water (DHW) system has been reported recently, with the solar collector being simulated by a zero-dimensional analytical model (Mongibello et al. 2014). In a zero-dimensional model the collector is treated as a single point with a single average temperature. One-dimensional numerical models were employed to find the temperature profile in the heat transfer fluid as well as in the water inside the hot water tank. The finite difference implicit scheme was utilized to solve for the energy balance in the coil heat exchanger and in the hot water tank. The energy conservation equations for the different solar DHW components were numerically coupled with the help of an implicit scheme based in-house computational code (Mongibello et al. 2014).

Implementation of advanced control techniques for the energy systems that rely upon the intermittent sources of heat energy (e.g. solar radiation), as well as, improvement in the overall efficiency necessitate computationally fast and, at the same time, adequately accurate system level dynamic models. Continued research effort in the direction of control-oriented modelling has resulted in the emergence of a particular category of simplified reduced-order models, formally classified as moving-boundary models (Eldredge and Alleyne 2006). Conventionally, for the physical systems that undergo a phase change at a specified temperature, the continuously shifting phase change boundary is detected by the means of a sweeping algorithm working over a region that is approximated and represented by a finite number of points. It is to be noted that there are significant challenges in obtaining accurate phase change boundaries using such a method. In order to improve the performance of the sweeping algorithm, a few solving techniques such as moving grid points and isotherm migration have been introduced, where specified isotherms are traced during their migration through the solution space, instead of determining the temperature at the spatial location and time instant of interest (Voller and Cross 1981; Wood 1991). However, well-formulated starting solutions are required to achieve meaningful results from the above-mentioned methods even in one-dimensional problems. Moving boundary method is capable of giving very accurate results over enthalpy methods without requiring well-formulated starting solutions, especially when the phase change takes over a very small temperature range or practically the process degenerates to a single temperature (Voller and Cross 1981). Therefore, in the context of solar thermal applications, low-order lumped parameter moving boundary models prove to be instrumental for the dynamical simulation of transient models and in determining the principal control parameters for the pivotal components, such as boilers and evaporators, where the phase change takes place in the working fluid side (Jensen and Tummescheit 2002; Zhang and Zhang 2006; Grald and MacArthur 1992; Shi et al. 2016). In such models, the flow of the working fluid inside the evaporator tube and the flow of the exhaust gas is considered to be one-dimensional. The pressure drop across the length of the evaporator is assumed to be negligible and this particular assumption leads to a reduced order model, as the need for momentum conservation goes away (Shi et al. 2016). The evaporator tube is considered to be thin, long and horizontal. The axial heat conduction is neglected in the working fluid as well as in the exhaust gas. The axial heat conduction in the tube wall is ignored as well. Another approach of convenience, in the context of renewable energy systems, is to use quasi-steady state models considering a reasonably large time step (~ 1 h) to facilitate ease of computation and validation, assuming the overall performance of the system to remain unfazed by the variability of the load and intermittency of the renewable sources within that time span (Hoevenaars and Crawford 2012).

12.2 Discussion About Specific Numerical Models

12.2.1 Modeling of Heat Exchanger (Boiler) in an ORC Based Solar Thermal Power Plant

In the foregoing discussion, numerical models of heat exchanger pertinent to solar thermal applications reported in published literature are elaborated. The first model describes a heat exchanger used as a boiler in an ORC based solar thermal power plant (Fig. 12.1) with a view to understanding its interaction with other components in the power plant for extending electricity generation after sunset (Lakhani et al. 2017). The aforesaid heat exchanger is modelled by assuming that the HTF enters a heating coil that passes through a tank of saturated liquid ORC, as shown in Fig. 12.2. The temperature of HTF inside the coil varies with time and distance along the coil while the temperature of organic fluid in the boiler is assumed to be constant during phase change.

The energy balance equation for the HTF in the coil is written as follows (Powell and Edgar 2012),

Fig. 12.1 Schematic diagram of ORC based solar thermal power plant with latent heat thermal storage system

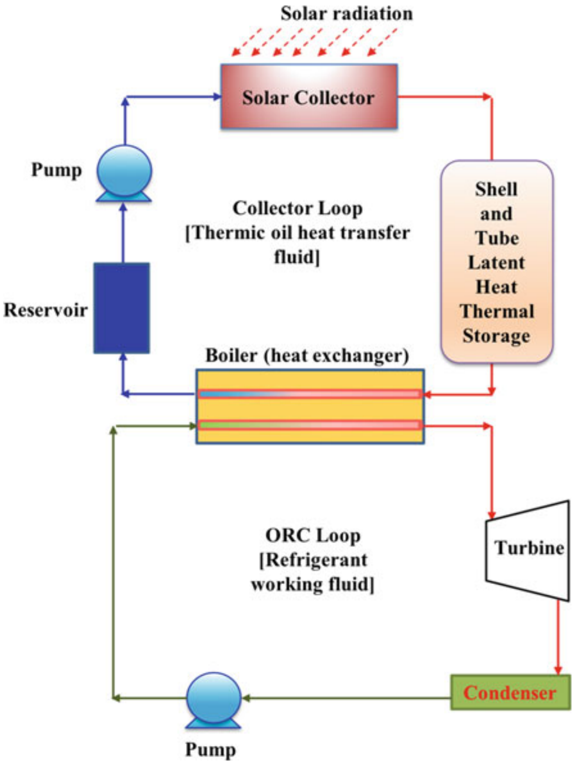

Fig. 12.2 Schematic diagram of heat exchanger (boiler)

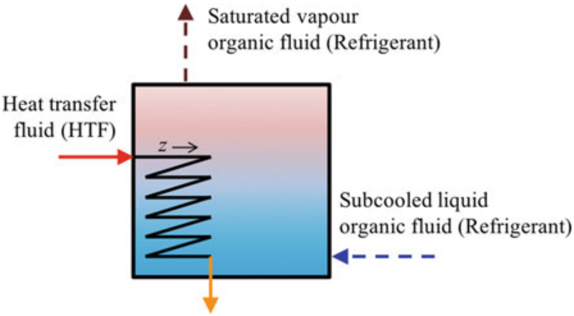

$$\rho_{\mathrm{HTF}} c_{p,\mathrm{HTF}} A_{b,i} \frac{\partial T_{\mathrm{HTF}}}{\partial t} + \dot{m}_{\mathrm{HTF}} c_{p,\mathrm{HTF}} \frac{\partial T_{\mathrm{HTF}}}{\partial z} = h_{\mathrm{conv},b} P_{b,i} (T_b - T_{\mathrm{HTF}}) \qquad (12.1)$$

where, z represents the distance along the boiler coil, T_b is the boiler organic fluid temperature and $A_{b,i}$ and $P_{b,i}$ represent the surface area and perimeter of the inner tube ($r_{p,i}$ = 0.03 m), respectively. The mass flow rate of the saturated organic fluid can be calculated from the steady-state energy balance on the boiler as,

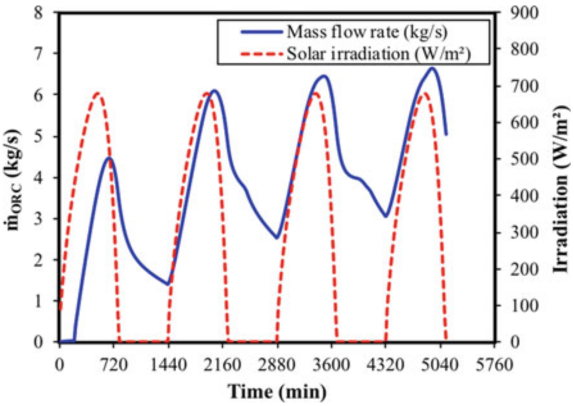

Fig. 12.3 Transient variation of solar irradiation and mass flow rate of organic fluid to generate 200 $\mathrm{kWh_t}$

$$\dot{m}_{\mathrm{HTF}} c_{p,\mathrm{HTF}} (T_{\mathrm{in}} - T_{\mathrm{out}}) = \dot{m}_{ORC} \left[h_{\mathrm{fg}} + \left(h_f - h_{\mathrm{sub},l} \right) \right] \tag{12.2}$$

where, h_{fg} is enthalpy of vaporization of the organic fluid at temperature T_b, h_f is the enthalpy of saturated organic fluid and $h_{\mathrm{sub},l}$ is the enthalpy of subcooled organic fluid.

Figure 12.3 shows the temporal variation in mass flow rate of organic fluid and solar radiation for four days of continuous operation of two-stage solar thermal power plant (Fig. 12.1). The parabolic solar collector of with dimensions 1500 (length) × 6 m (width) are considered for generating 200 $\mathrm{kWh_t}$ from the turbine. A shell and tube latent heat thermal storage system with representative dimension of shell diameter (D_i) of 98 mm, and HTF tube of $D_{i,\mathrm{HTF}}$ = 50 mm and $D_{o,\mathrm{HTF}}$ = 56 mm and total length of 4800 m is chosen in this study. An organic fluid R134a flows through the boiler tube of length 200 m and exchanges heat with Hytherm 600 (constant mass flow rate = 13.8 kg/s) in the collector loop. The ORC loop is pressurized at 3 MPa. The mass flow rate of organic fluid is observed to be varying with time according to the power output from the turbine. Details of the analysis can be found in (Lakhani et al. 2017).

12.2.2 Quasi Steady-State Reduced Order Moving Boundary Model for ORC Heat Exchanger

The second model of interest is the quasi steady-state reduced order moving boundary model for the medium temperature range (~120–200 °C) solar thermal applications. Recently reported work (Majumdar et al. 2018a) illustrated that a simplified quasi-steady state reduced order model is adequate for exhibiting the continuously changing phase change boundary characteristics in a narrow evaporator tube of a two-phase ORC heat exchanger. The model predicts the variation in ORC working fluid (refrigerant) mass flow rates with varying temperature of the commercial thermic oil employed as the heat transfer fluid to transfer heat content to the organic refrigerant (Majumdar et al. 2018a; Majumdar and Saha 2018) through the wall of the narrow evaporator tube. The average heat transfer fluid temperature (T_{HTF}) changes with the solar radiation incident on the solar collectors. The quasi-steady model enables prediction of the changes in temperature of the evaporator tube wall segments (subcooled, two-phase and superheated) with changing T_{HTF}. Very high tube wall segment temperatures have been predicted for the higher values of T_{HTF}. Additionally, the prescribed mass flow rates of the working fluid (refrigerant) have been found to very high as well, for higher values of T_{HTF}. Thus, the model serves as a useful tool for examining the viability of the operating conditions based on the temporal variation of the driving parameters, such as the solar radiation and T_{HTF}. The results of the quasi-steady model can be used as the initial guess in the computational algorithm developed for a detailed dynamic model, in order to explore the sharp transient characteristics by introducing time-dependent fluctuations in the subcooled refrigerant flow at the inlet of the two-phase ORC heat exchanger.

The quasi-steady state model was employed to investigate the moving boundary characteristics in the narrow evaporator tube of a two-phase ORC heat exchanger that carries an organic refrigerant. For the purpose of computational demonstration, a well-known and widely used hydrofluorocarbon compound named 1,1,1,2-Tetrafluoroethane (R134a), with a molecular formula: CH_2FCF_3 and formula weight of 102 kg/kmol, has been utilized (Vélez et al. 2014). The evaporator tube is placed inside a solar-thermal heat-exchanger (HE) reservoir (Fig. 12.4) that contains commercialized thermic oil (Hytherm 600), which is considered as HTF (Shinde et al. 2017). Fixed thermodynamic conditions of superheated refrigerant vapor have been assumed at the evaporator exit and the variation in refrigerant mass flow rate with changing temperature of heat transfer fluid (T_{HTF}) has been investigated for the chosen evaporator tube lengths of 5 and 10 m, respectively, with

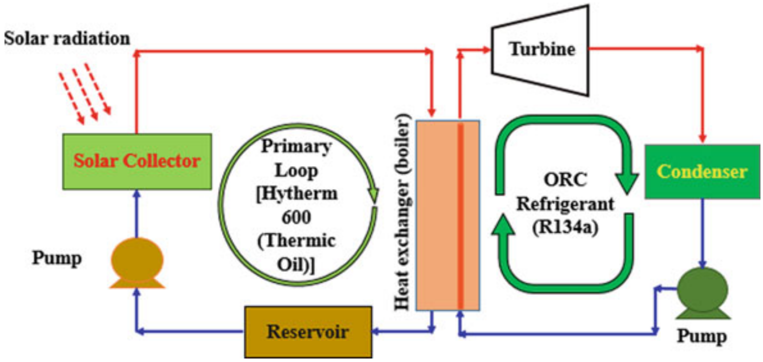

Fig. 12.4 Representative layout of the primary and secondary loops in a simplified ORC-based solar thermal power plant (Majumdar et al. 2018a). (Reproduced with permission from © 2018 Elsevier)

suitable constraints on the lengths of distinct flow segments (subcooled, two-phase and superheated).

The temperature of the thermic oil flowing in the collector loop is dependent on the level of available solar radiation. During a bright and cloudless day in India, the magnitude of solar radiation received at the earth surface (i.e. solar collector) increases with time and eventually reaches a peak value around noon. The solar radiation level decreases in the afternoon as the daylight diminishes and eventually ceases to exist in the evening. Therefore, during a diurnal solar radiation cycle, a rise phase is followed by a fall phase and this aspect needs to be taken into account in the time-dependent solar collector models. Relevant figures presented in the work by Lakhani et al. (Lakhani et al. 2017), shows that the heat transfer fluid temperature (T_{HTF}) keeps increasing as the intensity of the solar radiation increases and subsequently it reaches a maximum value as the solar radiation level reaches the diurnal peak. Thereafter, as the day progresses, the value of T_{HTF} decreases as the solar radiation level keeps diminishing. However, the value of T_{HTF} is found be considerably higher during the fall phase of solar radiation cycle than that observed during the rise phase for the same power level, due to different heat transfer rates (Majumdar et al. 2018a). The temperature of Hytherm 600 (HTF) at the collector outlet is calculated by assuming a fixed mass flow rate of 13.8 kg/s flowing through the collector loop (Fig. 12.4). The collector is modelled by following the parabolic trough configuration as described in the previously reported works (Powell and Edgar 2012; Behar et al. 2015). Figure 12.5 exhibits the temporal variation in HTF temperature (T_{HTF}) for the solar radiation data of Greater Noida, Uttar Pradesh, India; collected on June 2, 2016 (Lakhani et al. 2017; Majumdar et al. 2018a). For the illustrative computational results, the solar radiation profile stretching over a total time period of 640 min is used; where 7:20 AM in the morning is considered to be the starting time ($t = 0$) and the successive sample instances are separated by a uniform interval of 20 min (Majumdar et al. 2018a).

Conceptualization of phase change in the ORC heat exchanger. The schematic diagram of the evaporator tube (Fig. 12.6) exhibits three distinct phase segments of the working fluid, R134a. The evaporator tube is assumed to be placed

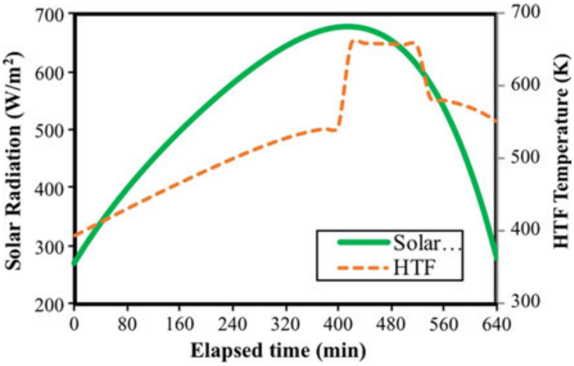

Fig. 12.5 Variation of the temperature of Hytherm 600 (T_{HTF}) with the representative diurnal solar radiation profile $\left(\tilde{P}_{\mathrm{solar}}\right)$ ($t = 0$ corresponds to 7:20 AM) (Majumdar et al. 2018a). (Reproduced with permission from © 2018 Elsevier)

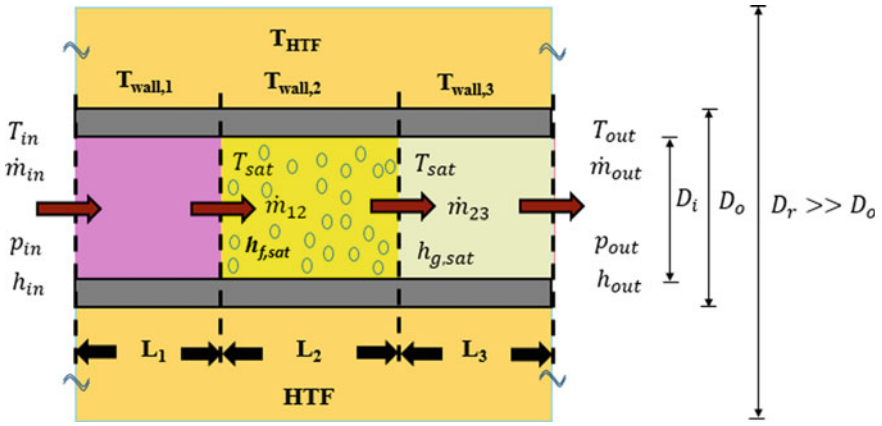

Fig. 12.6 Representative layout of the narrow evaporator tube placed in the thermic oil reservoir ($D_r \gg D_o$), (From left to right, the colored zones represent (i) sub-cooled segment, (ii) two-phase flow segment and (iii) superheated segment, respectively) (Majumdar et al. 2018a). (Reproduced with permission from © 2018 Elsevier)

inside a thermic oil reservoir with a diameter much greater than that of the evaporator tube, i.e. ($D_r \gg D_o$). Additionally, the thermal boundary layer thickness in the thermic oil side (δ) has been assumed to be considerably smaller than the annular span, i.e. $2\delta \ll (D_r - D_o)$. Furthermore, the thermic oil reservoir is assumed to be insulated on the outer surface. In an actual solar thermal power plant, a finite drop in the temperature is observed between the inlet and outlet of the thermic oil side in the heat exchanger employed in the load loop. This change in T_{HTF} takes place due to the transfer of heat content from the thermic oil (HTF) to the refrigerant (working fluid). However, the quasi-steady state reduced order moving boundary model assumes the simplification of an average value of the HTF temperature, and uses the linear average of the HTF temperatures at the inlet and the outlet of the ORC heat exchanger, respectively.

Computational set-up. For an illustrative computational demonstration of the quasi-steady reduced order moving boundary model in the two-phase load loop heat exchanger, evaporator tube lengths of 5 and 10 m have been chosen, as mentioned before. The operating pressure is assumed to be constant at 30 bar over the whole length of the heat-exchanger tube (*i.e.* $p_{\mathrm{in}} = p_{\mathrm{out}}$), and any change in pressure in the axial direction is neglected. This assumption prompts a quasi-steady operational condition. Subsequently, the mass flows across the various flow regimes can be equated to the steady state mass flow rate at the inlet of the ORC two-phase heat exchanger. The subcooled working fluid (refrigerant) enters the evaporator tube, where the subcooling margin ($T_{\mathrm{sat}} - T_{\mathrm{in}}$) is assumed to be approximately 40 °C. At length L_1 inside the evaporator tube (Fig. 12.6), the working fluid refrigerant becomes a saturated liquid, accompanied by a dryness fraction value of zero. The boiling begins at the axial location $L = L_1$, and the void fraction starts to increase. At the axial location $L = L_1 + L_2$, the flow becomes a completely dry, saturated steam. Thereafter, the dry refrigerant vapor gradually becomes superheated steam at 30 bar and acquires a significantly high temperature (T_{out}) as well as high specific enthalpy (h_{out}) at the exit of the evaporator tube and this superheated vapour enters the turbine.

Thermodynamically, R134a is an isentropic fluid and therefore the fluid flow at the turbine exit is assumed to be a saturated dry steam. The ambient temperature soars to about 45 °C during the scorching summer days in the western region of India. On top of that, it is assumed that there is a margin of temperature drop of 25 °C across the condenser unit. Therefore, upon taking into consideration the peak ambient temperature, the vapor temperature at the exit of the turbine is found as 70 °C. From the database of thermodynamic properties, the pressure at the exit of the turbine ($p_{\text{out,turbine}}$) is found to be 21.2 bar and the corresponding specific enthalpy at the turbine exit ($h_{\text{out,turbine}}$) is 280.48 kJ/kg (Majumdar et al. 2018a).

The flow enthalpy at the turbine inlet can be calculated using Eq. 12.3 as,

$$\left(\frac{\dot{W}_{\text{net}}}{\eta_{\text{isentropic}}}\right) = \dot{m}\left(h_{\text{in,turbine}} - h_{\text{out,turbine}}\right) \tag{12.3}$$

where, the isentropic efficiency ($\eta_{\text{isentropic}}$) of the turbine is chosen as 68.1% for a representative output power level of 200 kW_{t} (Sung et al. 2016). A representative steady state test mass flow rate value ($\dot{m} = 6.65\text{kg/s}$) is used, along with $\dot{W}_{\text{net}} = 200\,\text{kW}_{\text{t}}$ and the aforesaid calculated value of $h_{\text{out,turbine}}$; and the value of specific enthalpy at the turbine inlet $\left(h_{\text{in,turbine}}\right)$ is found to be 324.64 kJ/kg, which is equal to the specific enthalpy at the evaporator tube exit (h_{out}). The corresponding temperature of the superheated vapor (T_{out}) at 30 bar is approximately 364.31 K (Majumdar et al. 2018a).

Governing equations of quasi-steady moving boundary model. As the pressure gradient in the axial direction is neglected in the evaporator tube at the two-phase ORC heat exchanger, only mass and energy balances are considered in the reduced order modelling approach. The relevant equations are solved numerically for the average values of interest in the three distinct flow segments (subcooled, two-phase and the superheated), respectively; by treating each zone as a single node.

The general differential mass balance equation for a working fluid can be written as (Jensen and Tummescheit 2002),

$$\frac{\partial\rho}{\partial t} + \nabla \cdot (\rho\vec{v}) = 0 \tag{12.4}$$

where, ρ denotes density, t represents time and v symbolizes velocity.

For one-dimensional flow, Eq. 12.4 is reduced to,

$$\frac{\partial A\rho}{\partial t}+\frac{\partial \dot{m}}{\partial z}=0 \tag{12.5}$$

where, z represents the length traversed by the working fluid, t denotes time, $\dot{m}$ is the working fluid mass flow rate and A represents the cross-sectional area of the evaporator tube.

The general differential energy balance equation for a working fluid is given by,

$$\frac{\partial \rho h}{\partial t}+\nabla\cdot(\rho h\vec{v})=-\nabla.\vec{q}''-q'''+\frac{\mathrm{d}p}{\mathrm{d}t}+\varphi \tag{12.6}$$

where, h symbolizes specific enthalpy of the working fluid, φ denotes the dissipation function, $\vec{v}$ symbolizes the velocity, $\vec{q}''$ and q''' stand for is heat flux and the volumetric energy density, respectively.

For a one dimensional flow, the axial conductivity, radiation and the viscous stress terms are neglected for the sake of simplification in the energy balance, and hence, Eq. 12.6 can be rewritten as,

$$\frac{\partial(A\rho h-Ap)}{\partial t}+\frac{\partial \dot{m}h}{\partial z}=\pi D\alpha\left(T_{\text{wall}}-T_{\text{Rfg}}\right) \tag{12.7}$$

where, D is the inner diameter of the evaporator tube, α represents the average heat transfer coefficient, T_{wall} symbolizes the wall temperature and T_{Rfg} stands for the refrigerant bulk temperature.

The differential energy balance for the evaporator tube wall is obtained by simplifying Eq. 12.6, and upon neglecting the axial conductivity as well as the flow terms (Jensen and Tummescheit 2002), the required expression turns out to be,

$$c_{\text{wall}}A_{\text{wall}}\rho_{\text{wall}}\frac{\partial T_{\text{wall}}}{\partial t}=\alpha_i\pi D_i\left(T_{\text{Rfg}}-T_{\text{wall}}\right)+\alpha_o\pi D_o(T_{\text{HTF}}-T_{\text{wall}}) \tag{12.8}$$

where, c_{wall} stands for the heat capacity of the tube wall material, D_i and D_o symbolize the inner and outer diameter of the evaporator tube, respectively; ρ_{wall} represents the density of the tube wall material, A_{wall} represents total area of the evaporator tube wall, T_{HTF} stands for the average heat transfer fluid temperature around the evaporator tube, α_i and α_o symbolize the average inner and outer heat transfer coefficients of the evaporator tube, respectively.

Under a steady state operational condition, the conservation of fluid mass across all the flow segments, including the interfaces of the distinct flow regimes, gives,

$$\dot{m}_{\text{in}}=\dot{m}_{12}=\dot{m}_{23}=\dot{m}_{\text{out}} \tag{12.9}$$

where, $\dot{m}_{\text{in}}$ represents the mass flow rate subcooled refrigerant at the entry of the ORC two-phase heat exchanger, $\dot{m}_{12}$ and $\dot{m}_{23}$ represent the mass flow rates at the interfaces 1-2 and 2-3, respectively.

At the steady state condition, the energy balance equation in the subcooled region reduces to (Majumdar et al. 2018a; Majumdar and Saha 2018),

$$\dot{m}_{\text{in}} h_{\text{in}} - \dot{m}_{12} h_l(p) + \pi D_i \alpha_{i1} L_1 \left(T_{\text{wall},1} - \widetilde{T}_{\text{Rfg},1}\right) = 0 \tag{12.10}$$

where, h_{in} denotes the specific enthalpy of the subcooled refrigerant at the evaporator inlet, $h_l(p)$ represents the enthalpy of the saturated refrigerant fluid at the fluid interface 1-2; L_1 denotes the length of the subcooled flow segment, $T_{\text{wall},1}$ symbolizes the constant wall temperature of the subcooled segment, $\widetilde{T}_{\text{Rfg},1}$ stands for the average refrigerant temperature in the subcooled segment, α_{i1} denotes the average inner heat transfer coefficient in the subcooled segment.

Similarly, the energy balance equation for the two-phase region becomes,

$$\dot{m}_{12} h_l(p) - \dot{m}_{23} h_g(p) + \pi D_i \alpha_{i2} L_2 \left(T_{\text{wall},2} - \widetilde{T}_{\text{Rfg},2}\right) = 0 \tag{12.11}$$

where, $h_g(p)$ is the specific enthalpy of the saturated steam at the fluid interface 2-3; L_2 denotes the length of the two-phase flow segment, $T_{\text{wall},2}$ symbolizes the constant wall temperature of the two-phase segment, $\widetilde{T}_{\text{Rfg},2}$ stands for the average refrigerant temperature in the two-phase zone and α_{i2} represents the average inner heat transfer coefficient in the two-phase zone.

The energy balance in the superheated segment of the working fluid flow leads to,

$$\dot{m}_{23} h_g(p) - \dot{m}_{\text{out}} h_{\text{out}} + \pi D_i \alpha_{i3} L_3 \left(T_{\text{wall},3} - \widetilde{T}_{\text{Rfg},3}\right) = 0 \tag{12.12}$$

where, h_{out} stands for the specific enthalpy of the superheated steam at the outlet of the evaporator tube, L_3 symbolizes the length of the superheated flow segment, $T_{\text{wall},3}$ denotes tube wall temperature in the superheated segment, $\widetilde{T}_{\text{Rfg},3}$ symbolizes the average temperature of superheated refrigerant vapor and α_{i3} denotes the average inner heat transfer coefficient in the superheated region.

At a steady state condition, the energy balance equations for the evaporator tube wall corresponding to the three distinct flow segments can be obtained from Eq. 12.6, and are as below,

(a) In the subcooled region, the energy balance in the tube wall leads to,

$$\pi D_i \alpha_{i1} L_1 \left(\widetilde{T}_{\text{Rfg},1} - T_{\text{wall},1}\right) + \alpha_o \pi D_o L_1 \left(T_{\text{HTF}} - T_{\text{wall},1}\right) = 0 \tag{12.13}$$

(b) In the two-phase flow segment, the energy balance in the tube wall gives,

$$\pi D_i \alpha_{i2} L_2 \left(\widetilde{T}_{\mathrm{Rfg},2} - T_{\mathrm{wall},2}\right) + \alpha_o \pi D_o L_2 \left(T_{\mathrm{HTF}} - T_{\mathrm{wall},2}\right) = 0 \tag{12.14}$$

(c) In the superheated segment the relevant expression turns out to be,

$$\pi D_i \alpha_{i3} L_3 \left(\widetilde{T}_{\mathrm{Rfg},3} - T_{\mathrm{wall},3}\right) + \alpha_o \pi D_o L_3 \left(T_{\mathrm{HTF}} - T_{\mathrm{wall},3}\right) = 0 \tag{12.15}$$

The wall temperatures for the respective segments can be obtained by using Eqs. 12.13 to 12.15 for a quasi-steady operational condition. Thereafter, the wall temperatures are used to estimate the length of the respective flow regimes by utilizing Eqs. 12.10 to 12.12. For the above-mentioned calculation, the average temperature of the bulk refrigerant in each of the three flow regimes is required. The average temperatures in the flow segments of interest, $\widetilde{T}_{\mathrm{Rfg},1}$, $\widetilde{T}_{\mathrm{Rfg},2}$ and $\widetilde{T}_{\mathrm{Rfg},3}$, respectively, are calculated by utilizing the flow conditions specified at the inlet and outlet of the evaporator tube, as well as, the thermodynamic parameters corresponding to the saturation condition.

At the steady state pressure p, the specific volumes corresponding to the inlet temperature (T_{in}) and the saturation temperature (T_{sat}), respectively, can be obtained from the database of thermodynamic properties and hence, the densities can also be easily calculated as well.

Assuming the working fluid densities corresponding to the temperatures T_{in} and T_{sat} to be $\rho_1(0)$ and $\rho_1(L_1)$, respectively. The average density in the subcooled flow segment is calculated as (Majumdar et al. 2018a),

$$\overline{\rho_1} = \frac{2}{3}\rho_1(0) + \frac{1}{3}\rho_1(L_1) \tag{12.16}$$

Once the average density is found, the average temperature of the refrigerant in the subcooled flow segment, $\widetilde{T}_{\mathrm{rfg},1}$, can be obtained from the thermodynamic database. In the two-phase flow segment, the average refrigerant temperature $\widetilde{T}_{\mathrm{Rfg},2}$ is equal to the saturation temperature at the steady state pressure level p. In the superheated flow segment of length L_3, the average vapour temperature $\widetilde{T}_{\mathrm{Rfg},3}$ is calculated as (Majumdar et al. 2018a),

$$\widetilde{T}_{\mathrm{Rfg},3} = \frac{1}{3} T_{\mathrm{Rfg},3}(0) + \frac{2}{3} T_{\mathrm{Rfg},3}(L_3) \tag{12.17}$$

where, $T_{\mathrm{Rfg},3}(0)$ represents the saturation temperature at the steady state pressure level p, and $T_{\mathrm{Rfg},3}(L_3)$ denotes the temperature of the superheated vapour at the evaporator tube exit. These approximations are made with the assumption that the axial profiles of the temperature and the density of the ORC working fluid follow quadratic nature. However, more complicated profiles can be assumed for the working fluid with the inclusion of axial heat conduction and dissipation terms in the energy balance equation.

The prime focus of the quasi-steady moving boundary modelling approach is to find the lengths of the subcooled, two-phase and superheated segments in the narrow evaporator tube as well as the constant wall segment temperatures. From the mathematical formulation itself, it is quite evident that the heat transfer coefficient of a particular flow segment plays a very important role in determining length of that flow regime and also the constant tube wall temperature of that flow segment. It must be mentioned that the moving boundary model for one -dimensional fluid flow assumes an average inner heat transfer coefficient for each of the distinct flow segments of interest and also an average outer heat transfer coefficient (Jensen and Tummescheit 2002; Zhang and Zhang 2006; Grald and MacArthur 1992; Shi et al. 2016), as each of the sectional segments is represented by a single node.

Previously reported work, pertinent to the modeling and simulation of two-phase flow evaporators for parabolic-trough based solar thermal installations, mentions the application of the concept of heat transfer driven by an average heat transfer coefficient in each of the flow segments and approximation of regime-specific average heat transfer coefficient values (Cruz et al. 2013). Similar concept has also been utilized in control volume based object oriented modeling (Yebra 2006).

The Dittus-Boelter correlation is used to estimate the average inner heat transfer coefficient in the subcooled and superheated flow regimes (Dittus and Boelter 1930). For an average mass flow rate of 3 kg/s through the evaporator tube, the inner heat transfer coefficient for the subcooled segment, at the pumping pressure level of 3 MPa, is calculated to be 6071 $\mathrm{Wm}^{-2}\ \mathrm{K}^{-1}$, and that for the superheated region is calculated as 4868 $\mathrm{Wm}^{-2}\ \mathrm{K}^{-1}$. The calculated heat transfer coefficients are compared with the published experimental values (Li and Hrnjak 2017; Meyer 2014) and a good agreement is found. The calculated values of the heat transfer coefficient differ from the reported experimental values, as the experimental conditions (i.e. pressure, temperature, mass flow rate etc.) under which the heat transfer coefficients were measured are very different from those considered in the illustrative computational example.

It is noteworthy that the simplified reduced order quasi-steady model does not take into account the heat-flux transferred from the thermic oil side into the refrigerant flowing through the evaporator tube in the ORC heat exchanger. Furthermore, the reduced order modeling the study utilizes a time-invariant average void fraction for the two-phase region. Therefore, the average inner heat transfer coefficient in the two-phase region is iteratively calculated using Donowski-Kandlikar correlation (Donowski and Kandlikar 1999). For an average heat flux $\sim 900\ \mathrm{kWm}^{-2}$, an average operating refrigerant mass flow rate of 3 kg/s and by assuming an average void fraction of 0.665 (Jensen and Tummescheit 2002), the aforesaid heat transfer coefficient is estimated to be 25,058 $\mathrm{Wm}^{-2}\ \mathrm{K}^{-1}$.

The heat transfer coefficient of Hytherm 600 (HTF) is usually low and moreover, the thermophysical properties of this lubricant oil are not yet well characterized at temperatures in excess of 305 °C. The Gnielinski correlation (Gnielinski 1975), is used to estimate the outer heat transfer coefficient in the thermic oil side. For a thermic oil mass flow rate of 13.8 kg/s circulating in the primary loop (collector loop) and a thermic oil reservoir diameter (D_r) of 0.252 m, the average outer heat transfer coefficient is calculated to be 435 $\mathrm{Wm}^{-2}\ \mathrm{K}^{-1}$.

In order to ensure a sufficient length of subcooled segment (L_1) (for avoiding a dry out scenario), a working relationship between the refrigerant mass flow rate and the average temperature of Hytherm 600 (T_{HTF}) has been prescribed. The working relationship considers a finite length of the superheated region (L_3) as well, so that the saturated dry vapour is able to gain the required level of enthalpy at the evaporator outlet, in a gradual fashion. Once L_1 and L_3 are obtained, the length of the two-phase segment (L_2) can be found easily. Therefore, the length of the two-phase segment (L_2) is not constrained strictly. From the boundary condition applied on the rate of change of sectional lengths for evaluating the tube wall temperatures in the flow segments of interest (Jensen and Tummescheit 2002), it is quite evident that the length of the subcooled column increases with increasing refrigerant mass flux, whereas the length of the two-phase region shrinks. On the other hand, the two-phase segment broadens as soon as the subcooled segment begins to diminish due to the heat transfer from the thermic oil side and subsequent evaporation. The constraints applied on the sectional lengths depend on the several system parameters; such as the total length of the narrow evaporator tube (L), inner diameter of the evaporator tube (D_i), evaporator tube wall thickness ($D_o - D_i$), and the type of the refrigerant used. An empirical relationship is formed between the refrigerant (R134a) mass flow rate and T_{HTF} by using the aforementioned boundary conditions and constraints. The refrigerant mass flow rate of can neither be allowed to reach unfeasibly high values, nor it can be allowed to fall to an impractical low value based on the regular demand of the load loop. The mass inflow to the evaporator tube also depends on the capability of the pump used. In order to incorporate the effect of several system parameters, the scalar constants K_1 and K_2 are introduced in the relationship to achieve more accurate and situation specific values. Furthermore, the formulation also introduced offset correction constants K_3 and K_4 to aid fine-tuning of the working fluid mass flow rates, and these constants are to be determined iteratively in a case-specific manner. The upper limit as well as the lower limit of the working fluid mass flow rate are estimated to obtain a feasible operating range (Majumdar et al. 2018a).

In order to enable precise estimation of the mass flow rates, the constraints imposed on the sectional lengths should be varied as T_{HTF} and $\tilde{P}_{\mathrm{solar}}$ change. However, the same set of constraints is considered for the calculation of mass flow rates, over the whole range of values of T_{HTF}, for the sake of simplification in the numerical analysis. The flow-chart (Fig. 12.7) schematically shows the iterative process of estimating the mass flow rate of ORC working fluid.

The constraints imposed on the sectional lengths depends on the total length of the evaporator tube. Roughly, under normal operating conditions, the longer the evaporator tube, the longer should be length of the subcooled refrigerant segment. It must be noted that the refrigerant mass flow rate needs be increased to achieve a longer subcooled segment. With a view to obtaining the lower limit of the

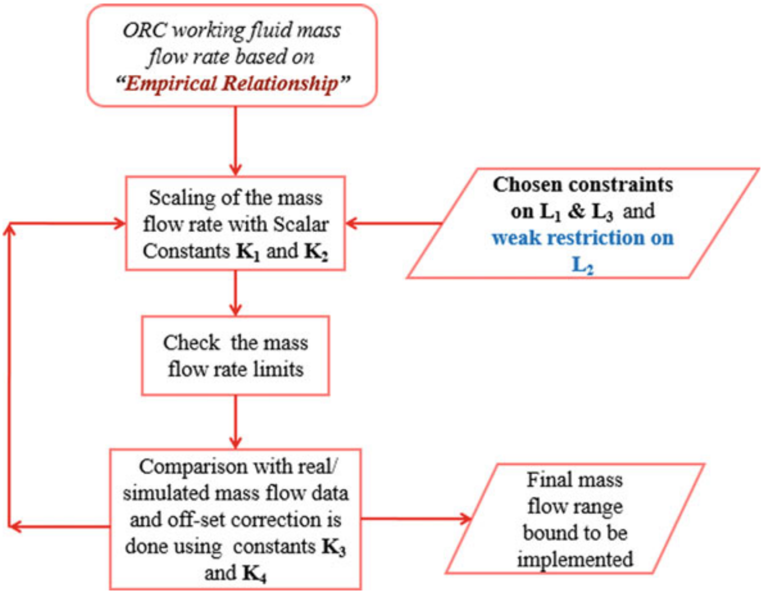

Fig. 12.7 A flow chart describing briefly the calculation of working fluid mass flow rates (Majumdar et al. 2018a). (Reproduced with permission from © 2018 Elsevier)

refrigerant mass flow rate $(\dot{m}_{\text{in}})$ for the 5 m long heat-exchanger tube, $L_1 \geq 2.5D_i, L_2 \geq 30D_i$ and $L_3 \geq 2.6D_i$ are assumed as the constraints on the sectional lengths. The upper limit of the mass flow rate for the evaporator tube is calculated by using the constraints $L_1 \geq 4.2D_i, L_2 \geq 186D_i$ and $L_3 \geq 4.5D_i$. On the other hand, for finding the lower limit of the refrigerant mass flow rate for the 10 m long evaporator tube, the constraints on the length segments are $L_1 \geq 2.8D_i, L_2 \geq 385D_i$ and $L_3 \geq 3.1D_i$; whereas, for the corresponding upper limit of the refrigerant mass flow rate, the assumed constraints are $L_1 \geq 5.1D_i, L_2 \geq 381D_i$ and $L_3 \geq 5.5D_i$.

The working relationships between the refrigerant mass flow rates $(\dot{m}_{\text{in}})$ and T_{HTF} are as follows (Majumdar et al. 2018a),

$$\dot{m}_{\text{in,lower}} = \underbrace{K_1\left(-1.019\times10^{-6}T_{\text{HTF}}^3 + 1.805\times10^{-3}T_{\text{HTF}}^2 - 0.8781T_{\text{HTF}} + 133.1\right)} + K_3 \tag{12.18}$$

$$\dot{m}_{\text{in,upper}} = \underbrace{K_2(0.237T_{\text{HTF}} - 84.0304)} + K_4 \tag{12.19}$$

In Eqs. 12.18 and 12.19, the empirical relationships between the refrigerant (R134a) mass flow rate and T_{HTF} are marked with accent. The empirical relationships are fine-tuned by using the added scalar constants, as described before.

For the purpose of convenient mathematical representation, separate ratios are defined for the sectional lengths of interest, L_1, L_2 and L_3, respectively, at the upper end as well as the lower end of the working fluid (R134a) mass flow rate. The lower and upper ends of the working fluid mass flow rate are given by Eqs. 12.20 and 12.21, respectively.

$$\dot{m}_{\text{in}} = \dot{m}_{\text{in,lower}} \tag{12.20}$$

$$\dot{m}_{\text{in}} = \dot{m}_{\text{in,upper}} \tag{12.21}$$

The aforementioned length ratios are defined as,

$$R_{j,\text{lower}} = \left(\frac{L_{j,\text{lower}}}{D_i}\right), \quad j = 1, 2, 3 \tag{12.22}$$

and

$$R_{j,\text{upper}} = \left(\frac{L_{j,\text{upper}}}{D_i}\right), \quad j = 1, 2, 3 \tag{12.23}$$

where, $L_{j,\text{lower}}$ and $L_{j,\text{upper}}$ symbolize the respective sectional lengths corresponding to the lower and upper ends of the working fluid mass flow rate, respectively.

Selected simulation results. Figure 12.8 demonstrates lower end and upper end mass flow rate profiles for the refrigerant (R134a), for both 5 m as well as 10 m long evaporator tubes, for the aforementioned computational set up as well as the imposed constraints on the sectional lengths (subcooled, two-phase, superheated). Corresponding length ratios can be found from Figs. 12.9, 12.10 and 12.11

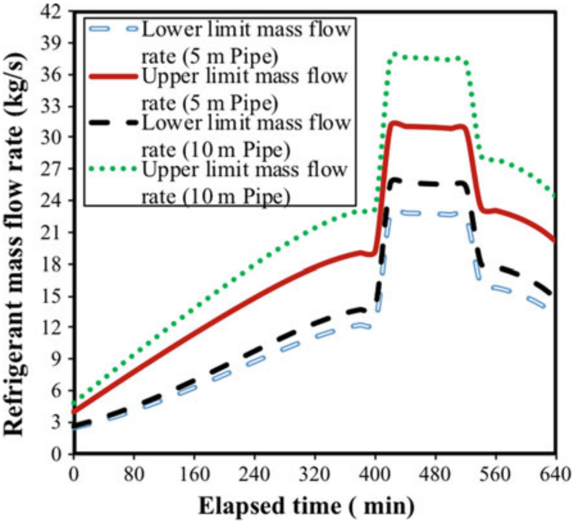

Fig. 12.8 Variation in the ORC refrigerant (R134a) mass flow rate with time-varying profile of T_{HTF} (t = 0 corresponds to 7:20 AM)

Fig. 12.9 Variation in the subcooled length ratio (R_1) with time-varying profile of T_{HTF} ($t = 0$ corresponds to 7:20 AM) (Majumdar et al. 2018a). (Reproduced with permission from © 2018 Elsevier)

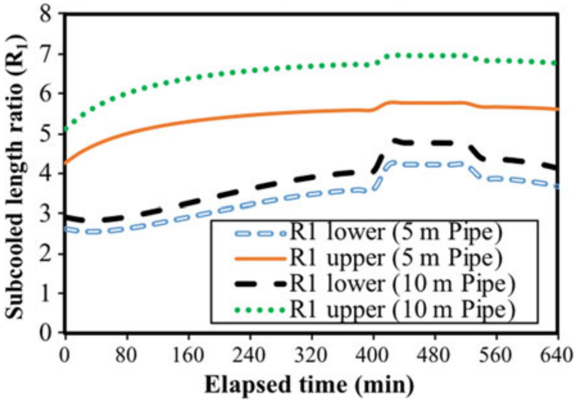

Fig. 12.10 Variation in the two-phase length ratio (R_2) with time-varying profile of T_{HTF} ($t = 0$ corresponds to 7:20 AM) (Majumdar et al. 2018a). (Reproduced with permission from © 2018 Elsevier)

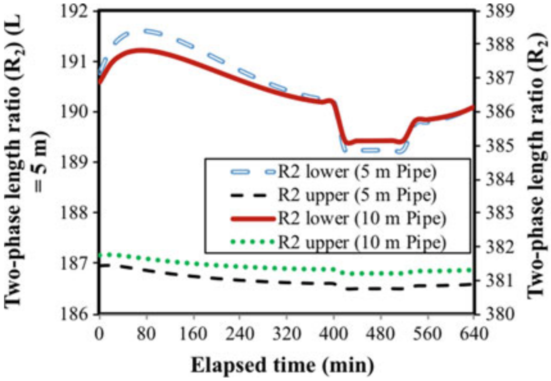

Fig. 12.11 Variation in the superheated length ratio (R_3) with time-varying profile of T_{HTF} ($t = 0$ corresponds to 7:20 AM)

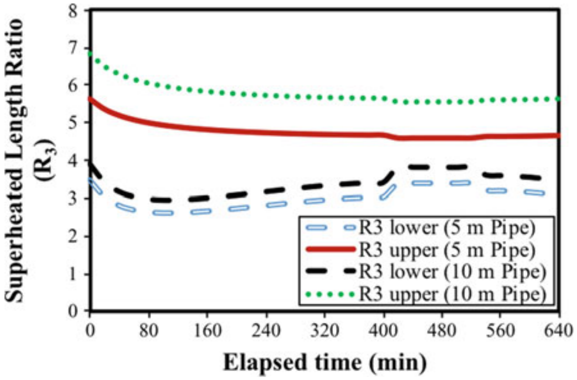

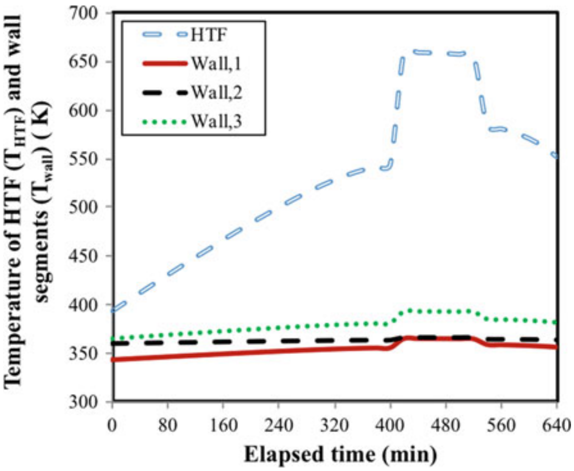

Fig. 12.12 Variation in the temperature of the wall segments ($T_{\text{wall},1}$, $T_{\text{wall},2}$, $T_{\text{wall},3}$) with time-varying profile of T_{HTF} ($t = 0$ corresponds to 7:20 AM)

respectively. The higher values of $R_{1,\text{lower}}$ and $R_{1,\text{upper}}$ in the middle region of the respective graphs in Fig. 12.9 indicate that the tube does not run dry at higher values of T_{HTF}. Figure 12.12 demonstrates the variation of temperatures of the wall segments ($T_{\text{wall},1}$, $T_{\text{wall},2}$, $T_{\text{wall},3}$) in response to the time-varying profile of T_{HTF}. From Figs. 12.5 and 12.12 respectively, it can be comprehended clearly that the wall temperature of the superheated flow segment ($T_{\text{wall},3}$) increases monotonically at the solar radiation level of about 250 W/m^2 during the rise phase. In the subcooled segment, the evaporator tube wall temperature ($T_{\text{wall},1}$) exhibits a comparably lower rate of increment with increasing values T_{HTF}. The wall temperature in the two-phase segment ($T_{\text{wall},2}$) hardly changes with increasing solar radiation. At the solar radiation levels of practical interest, the wall temperature of the subcooled region ($T_{\text{wall},1}$) is found to be the lowest of all three regions, whereas the tube wall in the superheated region turns out to be the hottest, i.e. $T_{\text{wall},1} < T_{\text{wall},2} < T_{\text{wall},3}$ (Fig. 12.12).

12.2.3 Dynamic Moving Boundary Reduced Order Model

From the preceding discussion, it can be evidently seen that quasi-steady models are very useful and effective in describing the long-time behavioral trends of the solar thermal systems. Nevertheless, the temporal fluctuations in the pumping pressure working on the subcooled working fluid cause prominent transient changes in the wall temperature profiles of the subcooled, two-phase and superheated segments of the narrow evaporator tube in the two-phase ORC heat exchanger. In order to address these transient changes, reasonably accurate and mathematically tractable system level dynamic models are required. Due to the computational speed as well as the simplicity of formulation, the moving boundary dynamic models have emerged as the front-runners in the context of advanced control of the solar thermal power plants (Majumdar et al. 2018b). For the dynamic moving boundary models to be applicable in the solar thermal applications as well as low-grade heat recovery systems, the assumptions of the evaporator tube and flow conditions remain the same as mentioned and discussed before (Shi et al. 2016; Majumdar et al. 2018b).

Governing equations. One-dimensional dynamic moving boundary model consists of the time-dependent mass balance and energy balance equations for the working fluid in each of the three distinct flow segments (subcooled, two-phase and superheated region) in the two-phase ORC heat exchanger. Additionally, three more equations are also required to account for the energy balance in the wall of the evaporator tube in each of the aforesaid segments. The time-varying operating pressure (pumping pressure), acting on the subcooled refrigerant (R134a) at the inlet of the two-phase evaporator, is considered to be the sole independent variable; whereas all other physical and thermodynamic variables of interest are taken as dependent variables (Majumdar et al. 2018b). This approach simplifies the mathematical formulation considerably and does away with the computational tediousness (Majumdar et al. 2018b), as reported in previously published work.

The mass balance equation for the subcooled region is written as,

$$A\left\{\left(\bar{\rho}_1(t)-\rho_{f,\mathrm{sat}}(t)\right)\frac{\mathrm{d}L_1(t)}{\mathrm{d}t}+L_1(t)\frac{\mathrm{d}\bar{\rho}_1(p)}{\mathrm{d}p}\frac{\mathrm{d}p(t)}{\mathrm{d}t}\right\}=\dot{m}_{\mathrm{in}}(t)-\dot{m}_{12}(t) \tag{12.24}$$

where, the time-dependent average density of the refrigerant in the subcooled segment at the pressure level $p(t)$ is expressed as, $\bar{\rho}_1(p(t))=\frac{2}{3}\rho_{f,\mathrm{in}}(p(t))+\frac{1}{3}\rho_{f,\mathrm{sat}}(p(t))$; by assuming a quadratic profile of variation in the working fluid density along the axial direction.

The mass balance equation for the two-phase flow segment is formulated as,

$$\begin{aligned}A\Bigg\{&\left(\rho_{f,\mathrm{sat}}(t)-\rho_{g,\mathrm{sat}}(t)\right)\frac{\mathrm{d}L_1(t)}{\mathrm{d}t}+(1-\bar{\gamma})\left(\rho_{f,\mathrm{sat}}(t)-\rho_{g,\mathrm{sat}}(t)\right)\frac{\mathrm{d}L_2(t)}{\mathrm{d}t}\\&+L_2(t)\left(\bar{\gamma}\frac{d\rho_{g,\mathrm{sat}}(p)}{\mathrm{d}p}+(1-\bar{\gamma})\frac{\mathrm{d}\rho_{f,\mathrm{sat}}(p)}{\mathrm{d}p}\right)\frac{\mathrm{d}p(t)}{\mathrm{d}t}\Bigg\}=\dot{m}_{12}(t)-\dot{m}_{23}(t)\end{aligned} \tag{12.25}$$

The flow qualities at the inlet as well as the at outlet of the evaporator tube are assumed to remain unchanged, and hence, the mean void fraction $(\bar{\gamma})$ can be assumed to be time-invariant (Wedekind et al. 1978; Beck and Wedekind 1981), i.e. $\frac{\mathrm{d}\bar{\gamma}}{dt}=0$.

The mass balance equation for the superheated flow segment is expressed as,

$$\begin{aligned}A\Bigg\{&L_3(t)\frac{\mathrm{d}\bar{\rho}_3(p)}{\mathrm{d}t}\frac{\mathrm{d}p(t)}{\mathrm{d}t}+\left(\rho_{g,\mathrm{sat}}(t)-\bar{\rho}_3(t)\right)\frac{\mathrm{d}L_1(t)}{\mathrm{d}t}\\&+\left(\rho_{g,\mathrm{sat}}(t)-\bar{\rho}_3(t)\right)\frac{\mathrm{d}L_2(t)}{\mathrm{d}t}\Bigg\}=\dot{m}_{23}(t)-\dot{m}_{\mathrm{out}}(t)\end{aligned} \tag{12.26}$$

The working fluid temperature at the outlet of the two-phase heat exchanger ($T_{\mathrm{out,HE}}$) is assumed to be remain fixed irrespective of the inlet conditions (Majumdar et al. 2018b). The time-varying average temperature of the working fluid in the superheated segment $\left(\widetilde{T}_{\mathrm{Rfg},3}(t)\right)$ is formulated as, $\widetilde{T}_{\mathrm{Rfg},3}(t) = \frac{1}{3}T_{f,\mathrm{sat}}(t) + \frac{2}{3}T_{\mathrm{out,HE}}$; $T_{f,\mathrm{sat}}(t)$ symbolizes the saturation temperature of the working fluid refrigerant corresponding to the time-varying pumping pressure $P(t)$ at the evaporator inlet.

The dynamical energy balance equation for the subcooled flow segment is formulated as,

$$\begin{aligned} &A\left\{ \left(\bar{\rho}_1(t)\bar{h}_1(t) - \rho_{f,\mathrm{sat}}(t)h_{f,\mathrm{sat}}(t)\right)\frac{\mathrm{d}L_1(t)}{\mathrm{d}t} \right. \\ &\quad \left. + \left(L_1(t)\bar{\rho}_1(t)\frac{\mathrm{d}\bar{h}_1(p)}{\mathrm{d}p} + L_1(t)\bar{h}_1(t)\frac{\mathrm{d}\bar{\rho}_1(p)}{\mathrm{d}p} - L_1(t)\right)\frac{\mathrm{d}p(t)}{\mathrm{d}t} \right\} \\ &\quad + \dot{m}_{12}(t)h_{f,\mathrm{sat}}(t) - \dot{m}_{\mathrm{in}}(t)h_{\mathrm{in}}(t) = \pi D_i \alpha_{i1} L_1(t) T_{\mathrm{wall},1}(t) - \widetilde{T}_{\mathrm{Rfg},1}(t) \end{aligned} \tag{12.27}$$

The values of average specific enthalpy $(\bar{h}_1(t))$ is found by using the average density in the subcooled flow segment $(\bar{\rho}_1(t))$ (IRC Online Fluid Property Calculator 2018). The average temperature of the refrigerant in the subcooled zone $\left(T_{\mathrm{Rfg},1}(t)\right)$ is found by utilizing the values of $(\bar{\rho}_1(t))$ (Isobaric Properties for Ethane 2018).

The dynamical energy balance equation for the two-phase flow segment is written as,

$$\begin{aligned} &A\left[L_2(t)\left\{\bar{\gamma}\rho_{g,\mathrm{sat}}(t)\frac{\mathrm{d}h_{g,\mathrm{sat}}(p)}{\mathrm{d}p} + \bar{\gamma}h_{g,\mathrm{sat}}(t)\frac{\mathrm{d}\rho_{g,\mathrm{sat}}(p)}{\mathrm{d}p}\right.\right. \\ &\quad \left. + (1-\bar{\gamma})\rho_{f,\mathrm{sat}}(t)\frac{\mathrm{d}h_{f,\mathrm{sat}}(p)}{\mathrm{d}p} + (1-\bar{\gamma})h_{f,\mathrm{sat}}(t)\frac{\mathrm{d}\rho_{f,\mathrm{sat}}(p)}{\mathrm{d}p} - 1\right\}\frac{\mathrm{d}p(t)}{\mathrm{d}t} \\ &\quad + \left\{\bar{\gamma}\rho_{g,\mathrm{sat}}(t)h_{g,\mathrm{sat}}(t) + (1-\bar{\gamma})\rho_{f,\mathrm{sat}}(t)h_{f,\mathrm{sat}}(t)\right\}\frac{\mathrm{d}L_1(t)}{\mathrm{d}t} \\ &\quad \left. + \left\{(1-\bar{\gamma})\left(\rho_{f,\mathrm{sat}}(t)h_{f,\mathrm{sat}}(t) - \rho_{g,\mathrm{sat}}(t)h_{g,\mathrm{sat}}(t)\right)\right\}\frac{\mathrm{d}L_2(t)}{\mathrm{d}t}\right] \\ &\quad + \dot{m}_{23}(t)h_{g,\mathrm{sat}}(t) - \dot{m}_{12}(t)h_{f,\mathrm{sat}}(t) = \pi D_i \alpha_{i2} L_2(t) T_{\mathrm{wall},2}(t) - \widetilde{T}_{\mathrm{Rfg},2}(t) \end{aligned} \tag{12.28}$$

The energy balance equation pertinent to the superheated flow is formulated as,

$$\begin{aligned} &A\left\{\bar{\rho}_3(t)\bar{h}_3(t)\frac{\mathrm{d}L_3(t)}{\mathrm{d}t} + \rho_{g,\mathrm{sat}}(t)h_{g,\mathrm{sat}}(t)\frac{\mathrm{d}L_2(t)}{\mathrm{d}t}L_3(t)\right. \\ &\quad \left. + \left(\bar{\rho}_3(t)\frac{\mathrm{d}\bar{h}_3(p)}{\mathrm{d}p} + L_3(t)\bar{h}_3(t)\frac{\mathrm{d}\bar{\rho}_3(p)}{\mathrm{d}p} + - L_3(t)\right)\frac{\mathrm{d}p(t)}{\mathrm{d}t}\right\} \\ &\quad + \dot{m}_{\mathrm{out}}(t)h_{\mathrm{out}}(t) - \dot{m}_{23}(t)h_{g,\mathrm{sat}}(t) = \pi D_i \alpha_{i3} L_3(t) T_{\mathrm{wall},3}(t) - \widetilde{T}_{\mathrm{Rfg},3}(t) \end{aligned} \tag{12.29}$$

where, the average density of the refrigerant vapour in the superheated flow segment ($\bar{\rho}_3(t)$) is found by utilizing $\widetilde{T}_{\mathrm{Rfg},3}(t)$ along with $p(t)$ (Isobaric Properties for Ethane 2018). Thereafter, $\bar{\rho}_3(t)$ is utilized along with $p(t)$ to find $\bar{h}_3(t)$ from the database of thermodynamic values (IRC Online Fluid Property Calculator 2018). The density ($\rho_{\mathrm{out}}(t)$) and the specific enthalpy ($h_{\mathrm{out}}(t)$) of superheated refrigerant vapour at the exit of the two-phase heat exchanger, are found by using the fixed temperature of the working fluid at the heat exchanger outlet ($T_{\mathrm{out,HE}}$) (Isobaric Properties for Ethane 2018) and transient pressure $p(t)$.

The energy balance equation for the tube wall of the subcooled segment is given is,

$$\begin{aligned} & c_{\mathrm{wall}}\rho_{\mathrm{wall}}A_{\mathrm{wall}}\left\{L_1\frac{dT_{\mathrm{wall},1}(t)}{\mathrm{d}t} + \left(T_{\mathrm{wall},1}(t) - T_{\mathrm{wall},1,\mathrm{end}}(t)\right)\frac{\mathrm{d}L_1(t)}{\mathrm{d}t}\right\} \\ & = \alpha_{i1}\pi D_i L_1(t)\left(\tilde{\mathrm{T}}_{\mathrm{Rfg},1}(t) - T_{\mathrm{wall},1}(t)\right) + \alpha_o \pi D_o L_1(t)\left(\tilde{\mathrm{T}}_{\mathrm{HTF}}(t) - T_{\mathrm{wall},1}(t)\right) \end{aligned} \tag{12.30}$$

where, $A_{\mathrm{wall}} = \pi(D_o - D_i)$; $T_{\mathrm{wall},1,\mathrm{end}}(t) = T_{\mathrm{wall},1}(t)|_{z=L_1(t)}$.

The average HTF temperature $\left(\widetilde{T}_{\mathrm{HTF}}(t)\right)$ is altered by changing the HTF mass flow rate, which in turn is modulated according to the circulating mass flow rate of the pressurized feed water in the collector loop or the primary heat transfer loop (Majumdar et al. 2018b).

The dynamical energy balance equation for the wall of the two-phase flow segment of evaporator tube is,

$$\begin{aligned} & c_{\mathrm{wall}}\rho_{\mathrm{wall}}A_{\mathrm{wall}}\left\{\begin{array}{l} L_2(t)\frac{\mathrm{d}T_{\mathrm{wall},2}(t)}{\mathrm{d}t} + \left(T_{\mathrm{wall},1,\mathrm{end}}(t) - T_{\mathrm{wall},2}(t)\right)\frac{\mathrm{d}L_1(t)}{\mathrm{d}t} \\ + \left(T_{\mathrm{wall},2}(t) - T_{\mathrm{wall},2,\mathrm{end}}(t)\right)\frac{\mathrm{d}L_2(t)}{\mathrm{d}t} \end{array}\right\} \\ & = \alpha_{i2}\pi D_i L_2(t)\left(\widetilde{\mathrm{T}}_{\mathrm{Rfg},2}(t) - T_{\mathrm{wall},2}(t)\right) + \alpha_o \pi D_o L_2(t)\left(\widetilde{\mathrm{T}}_{\mathrm{HTF}}(t) - T_{\mathrm{wall},2}(t)\right) \end{aligned} \tag{12.31}$$

where, $T_{\mathrm{wall},2,\mathrm{end}}(t) = T_{\mathrm{wall},2}(t)|_{z=L_1(t)+L_2(t)}$ and the boundary condition is taken as (Jensen and Tummescheit 2002),

$$\left.\begin{array}{ll} T_{\mathrm{wall},2,\mathrm{end}}(t) = T_{\mathrm{wall},2}(t) & if\ \frac{dL_2(t)}{\mathrm{d}t} \leq 0 \\ T_{\mathrm{wall},2,\mathrm{end}}(t) = T_{\mathrm{wall},3}(t) & if\ \frac{\mathrm{d}L_2(t)}{dt} > 0 \end{array}\right\} \tag{12.32}$$

and

$$\left.\begin{array}{ll} T_{\mathrm{wall},1,\mathrm{end}}(t) = T_{\mathrm{wall},1}(t) & if\ \frac{\mathrm{d}L_1(t)}{\mathrm{d}t} \leq 0 \\ T_{\mathrm{wall},1,\mathrm{end}}(t) = T_{\mathrm{wall},2}(t) & if\ \frac{\mathrm{d}L_1(t)}{\mathrm{d}t} > 0 \end{array}\right\} \tag{12.33}$$

The energy balance equation for the wall of the superheated region of heat exchanger tube is given as,

$$\begin{aligned} & c_{\text{wall}}\rho_{\text{wall}}A_{\text{wall}}\left\{L_3\frac{dT_{\text{wall},3}(t)}{\mathrm{d}t} + \left(T_{\text{wall},1,\text{end}}(t) - T_{\text{wall},2}(t)\right)\frac{\mathrm{d}L_1(t)}{\mathrm{d}t}\right. \\ & \quad \left. + \left(T_{\text{wall},2,\text{end}}(t) - T_{\text{wall},3}(t)\right)\left(\frac{\mathrm{d}L_1(t)}{dt} + \frac{\mathrm{d}L_2(t)}{\mathrm{d}t}\right)\right\} \\ & = \alpha_{i3}\pi D_i L_3(t)\left(\tilde{\mathrm{T}}_{\text{Rfg},3}(t) - T_{\text{wall},3}(t)\right) + \alpha_o \pi D_o L_3(t)\left(\tilde{\mathrm{T}}_{\text{HTF}}(t) - T_{\text{wall},3}(t)\right) \end{aligned} \tag{12.34}$$

The boundary condition is given as (Jensen and Tummescheit 2002),

$$\left.\begin{aligned} T_{\text{wall},2,\text{end}}(t) = T_{\text{wall},2}(t) \quad & if\ \tfrac{dL_2(t)}{\mathrm{d}t} \leq 0 \\ T_{\text{wall},2,\text{end}}(t) = T_{\text{wall},3}(t) \quad & if\ \tfrac{\mathrm{d}L_2(t)}{\mathrm{d}t} > 0 \end{aligned}\right\} \tag{12.35}$$

and

$$\left.\begin{aligned} T_{\text{wall},1,\text{end}}(t) = T_{\text{wall},1}(t) \quad & if\ \tfrac{\mathrm{d}L_1(t)}{\mathrm{d}t} \leq 0 \\ T_{\text{wall},1,\text{end}}(t) = T_{\text{wall},2}(t) \quad & if\ \tfrac{\mathrm{d}L_1(t)}{\mathrm{d}t} > 0 \end{aligned}\right\} \tag{12.36}$$

Selected computational results for the transient model. In order to facilitate the demonstration of the transient characteristics of the dynamic model, a sinusoidal profile for the pumping pressure is assumed. The mathematical expression for the time-varying pressure is given by following the footsteps of relevant mathematical formulation available in published literature (Desideri et al. 2016),

$$p(t) = p_o\left[1 + 0.01\left(\frac{PPS}{2}\right)\sin(0.3 \times 2\pi t)\right] \tag{12.37}$$

where, PPS denotes the envelope (in number of percentage) encompassing the peak-to-peak deviation from the mean pressure. In the representative results, an envelope of 0.1% peak-to-peak deviation is assumed about the mean operating pressure (p_o), and therefore PPS = 0.1.

In order to solve for the governing Eqs. (12.24)–(12.31) and (12.34), the initial conditions (at $t = 0$) are obtained from the numerical results of the quasi-steady model. The constraints on the length segments are suitably chosen such that a subcooled segment length (L_1) of at least $0.015L$ is always ensured across the time-varying profile of $\widetilde{T}_{\text{HTF}}(t)$, in order to ensure that the evaporator tube in the two-phase ORC heat exchanger never faces a dearth of subcooled column. Furthermore, a superheated segment length (L_3) of at least $0.0467L$ is ensured as well, to facilitate the desired level of specific enthalpy of the superheated vapour at the outlet of the evaporator tube, at 30 bar. The initial values for the wall segment temperatures ($T_{\text{wall},1}$, $T_{\text{wall},2}$ and $T_{\text{wall},3}$) are chosen as 395, 370 and 430 K, respectively, following the steady state values reported in an earlier work

(Jensen and Tummescheit 2002). Detailed description of the computational scheme can be found in the relevant published work (Majumdar et al. 2018b).

The dynamical simulation of the one-dimensional model demonstrated that the transient fluctuations in the temperatures of the tube wall segments are essentially of similar graphical nature to the fluctuations in the pumping pressure at the inlet of the two-phase evaporator (Majumdar et al. 2018b). Similar observations were found in earlier computational works pertaining to the modeling and simulation of two-phase flows (Bauer 1999).

Figures 12.13, 12.14 and 12.15 represent the transient variations of the wall temperatures of the subcooled, two-phase and superheated segments of the evaporator tube of the two-phase ORC heat exchanger, respectively, for a suitable mass inflow rate of the subcooled ORC refrigerant which will enable generation of at least 750 kWt at the turbine. In the reported work (Majumdar et al. 2018b), while calculating the output power it was assumed that the mass flow rate of the superheated refrigerant steam remains almost the same as the mass flow rate of the subcooled refrigerant entering the narrow evaporator tube. From Figs. 12.13, 12.14, 12.15 it can be evidently observed that the temporal fluctuations in the wall temperature is the largest in the superheated region, whereas the temperature swing is found to be the lowest in the two-phase region. Very sharp transient variations in the wall temperatures of interest is a computational artefact that arise from one of the key assumptions used in the formulation of the moving boundary dynamic model that the axial heat conduction in the tube wall is neglected.

More accurate results can be obtained with proper thermal optimization of the system based on the length on the evaporator tube, working fluid mass flow rate and the heat flux transferred into the working fluid from the hot thermic oil side.

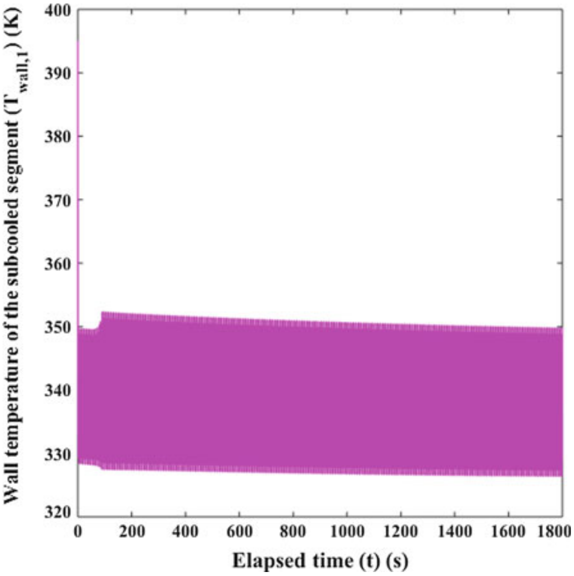

Fig. 12.13 Transient fluctuations in the subcooled region wall temperature ($T_{\mathrm{wall},1}$) (Majumdar et al. 2018b). (Reproduced with permission from © 2018 Elsevier)

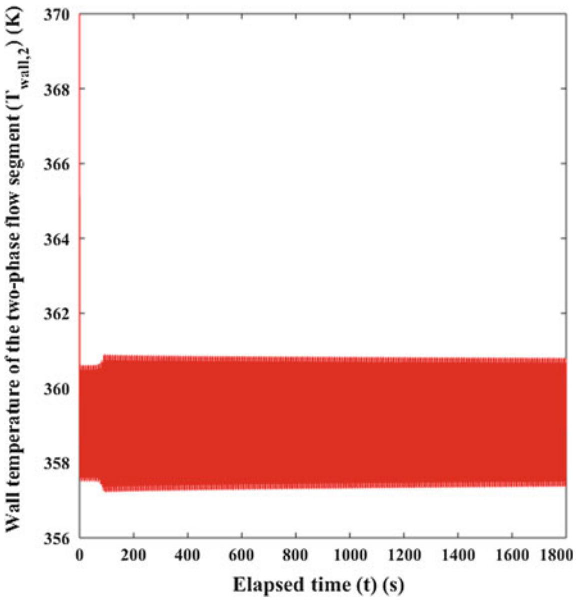

Fig. 12.14 Transient fluctuations in the two-phase region wall temperature ($T_{wall,2}$) (Majumdar et al. 2018b). (Reproduced with permission from © 2018 Elsevier)

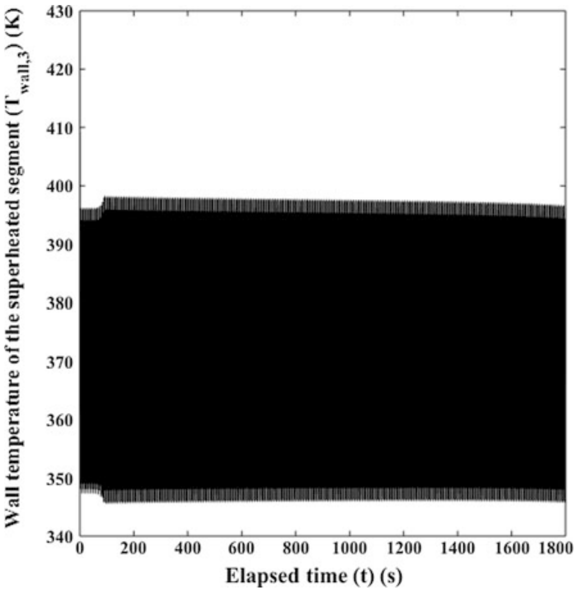

Fig. 12.15 Transient fluctuations in the superheated region wall temperature ($T_{wall,3}$) (Majumdar et al. 2018b). (Reproduced with permission from © 2018 Elsevier)

12.2.4 Moving Boundary Dynamic Model with Inclusion of Momentum Conservation

Momentum conservation equation is introduced to the transient moving boundary model (Jensen and Tummescheit 2002) in order to take into account the effect of pressure drop across the long evaporator tube with a length of the order of 1000 m in real life solar thermal installations. The model is formulated based on the Finite Volume Method (FVM) using staggered grid control volume approach. Figure 12.16 shows the computational control volume with three different regions of the fluid. The following hypotheses are made in the model to incorporate the pressure changing over the successive flow regions (subcooled, two-phase and superheated sections) represented by $P_o(t)$, $P_1(t)$ and $P_2(t)$ in the respective control volumes (figure). A tilt angle (α) over the horizontal plane has also been considered. The mass and energy conservations are made in the control volume $CV_{M,Ei}$ whereas the control volume, $CV_{\mathrm{FM},i}$ is used for the momentum conservation. The temporal evaluation of control volume boundaries is discussed in detail in the work reported by Yebra (Yebra et al. 2005). The General Balance Equation (GBE) is expressed as (Jensen and Tummescheit 2002; Todreas and Kazimi 1993),

$$\frac{\mathrm{d}}{\mathrm{d}t}\int\limits_{\forall}\rho\zeta\mathrm{d}\forall+\oint\limits_{S}\rho\zeta(u-u_s)\hat{n}\mathrm{d}S=\int\limits_{\forall}\rho\phi\mathrm{d}\forall+\oint\limits_{S}J\hat{n}\mathrm{d}S \tag{12.38}$$

where u is the fluid velocity, u_s is the CV surface velocity and $\hat{n}$ is the unit normal vector to CV surface. The variables $\{\zeta,\phi,J\}$ takes the form according to the conservation equation as tabulated in Table 12.1. In Table 12.1, g is the

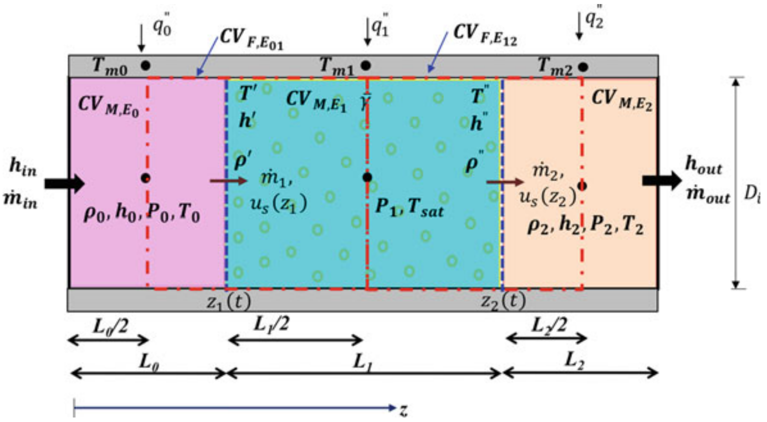

Fig. 12.16 Computational domain divided into control volumes (dash-dotted lines indicate staggered grid and dotted lines designate standard grid)

Table 12.1 Variables $\{\zeta, \phi, J\}$ in the conservation equations

Conservation equation	ζ	ϕ	J
Mass	1	0	0
Momentum	u	g	$\bar{\tau} - P\bar{I}$
Energy	$e + \frac{u^2}{2}$	gu	$-q'' + (\bar{\tau} - P\bar{I})u$

acceleration due to gravity, τ is the surface stress tensor, I is the identity matrix, q'' is the energy flux on the surface S, P is the pressure and e is the specific internal energy.

Momentum conservation:

The one-dimensional momentum conservation in z-direction of evaporator with cross section A, can be written as,

$$\begin{aligned} &A\frac{\mathrm{d}\left(\overline{\rho\zeta}\right)}{\mathrm{d}t}(z_2 - z_1) + A\left(\overline{\rho\zeta}\right)\left(\frac{\mathrm{d}z_2}{\mathrm{d}t} - \frac{\mathrm{d}z_1}{\mathrm{d}t}\right) \\ &+ A\left[\left(\rho\zeta(u - u_s)\right)\big|_{z_2} - \left(\rho\zeta(u - u_s)\right)\big|_{z_1}\right] \\ &= A\int_{z_1}^{z_2} \rho\phi dz + \oint_S J\hat{n}\mathrm{d}S \end{aligned} \tag{12.39}$$

For $u_s|_{z_i} = \frac{\mathrm{d}z_i}{\mathrm{d}t}$. The momentum conservation equation turns out to be after substituting the variables $\{\zeta, \phi, J\}$,

$$\begin{aligned} &(z_2 - z_1)\frac{\mathrm{d}\bar{\dot{m}}}{\mathrm{d}t} + \left(\dot{m}(z_1) - \bar{\dot{m}}\right)\frac{\mathrm{d}z_1}{\mathrm{d}t} - \left(\dot{m}(z_2) - \bar{\dot{m}}\right)\frac{\mathrm{d}z_2}{\mathrm{d}t} \\ &= \dot{I}(z_1) - \dot{I}(z_2) - A\rho g(z_2 - z_1)\sin\alpha - AP_{loss} \\ &+ A(P(z_2) - P(z_1)) \end{aligned} \tag{12.40}$$

where, $\bar{\dot{m}}$ is the average mass flow rate in the interval $[z_1, z_2]$ and is expressed as $\frac{1}{(z_2 - z_1)}A\int_{z_1}^{z_2} \dot{m}(z)\mathrm{d}z$ and the mass flow rate $\dot{m}(z_i)$ is calculated at z_i. The momentum flux, $\dot{I}(z_i)$ can be evaluated at z_i using $\dot{m}(z_i)|u(z_i)|$. The equivalent pressure of friction forces in control volume can be determined assuming turbulent flow as $P_{\mathrm{loss}} = f\frac{(z_2 - z_1)\bar{\dot{m}}|\bar{\dot{m}}|}{2A^2\rho\left(\bar{\dot{m}}\right)D_{\mathrm{in}}}$. $\rho\left(\bar{\dot{m}}\right)$ takes the form according to the discretization scheme, such as central difference or upwind. The parameters, $P(z_i), f$ and D_{in} are pressure at z_i, friction factor and hydraulic diameter, respectively. For two consecutive control volumes, the terms used in Eq. (12.40) have been summarized in Table 12.2.

The momentum equation is solved using the following boundary conditions on CV_{M,E_i}-

Table 12.2 Terms used in Eq. (12.40) for two control volumes $CV_{FM_{0-1}}$ and $CV_{FM_{1-2}}$

Variable	$CV_{FM_{0-1}}$	$CV_{FM_{1-2}}$
z_1	$\frac{L_0}{2}$	$L_0 + \frac{L_1}{2}$
z_2	$L_0 + \frac{L_1}{2}$	$L_0 + L_1 + \frac{L_2}{2}$
$\overline{\dot{m}}$	$\dot{m}_1$	$\dot{m}_2$
$\dot{I}(z_1)$	$\frac{\overline{\dot{m}}(z_1)\lvert\overline{\dot{m}}(z_1)\rvert}{A\rho_0}$	$\frac{\overline{\dot{m}}(z_1)\lvert\overline{\dot{m}}(z_1)\rvert}{A\rho_1}$
$\dot{I}(z_2)$	$\frac{\overline{\dot{m}}(z_2)\lvert\overline{\dot{m}}(z_2)\rvert}{A\rho_1}$	$\frac{\overline{\dot{m}}(z_2)\lvert\overline{\dot{m}}(z_2)\rvert}{A\rho_2}$
$P(z_1)$	P_0	P_1
$P(z_2)$	P_1	P_2
P_{loss}	$f\frac{(L_0-L_1)\dot{m}_1\lvert\dot{m}_1\rvert}{4A^2\rho(\dot{m}_1)D_{\text{in}}}$	$f\frac{(L_1-L_2)\dot{m}_2\lvert\dot{m}_2\rvert}{4A^2\rho(\dot{m}_2)D_{\text{in}}}$
$\rho(\dot{m}_1)$	$\frac{\rho_0+\rho_1}{2}$	
$\rho(\dot{m}_2)$		$\frac{\rho_1+\rho_2}{2}$
$\dot{m}(z_1)$	$\frac{\dot{m}_{\text{in}}+\dot{m}_1}{2}$	$\frac{\dot{m}_1+\dot{m}_2}{2}$
$\dot{m}(z_2)$	$\frac{\dot{m}_1+\dot{m}_2}{2}$	$\frac{\dot{m}_2+\dot{m}_{\text{out}}}{2}$

$$P(L_0) = \frac{P_0+P_1}{2}; P(L_0+L_1) = \frac{P_1+P_2}{2} \tag{12.41}$$

$$T_w(L_0) = \begin{cases} T_{w0} & \text{if } \frac{\mathrm{d}L_0}{\mathrm{d}t} > 0 \\ T_{w0} & \text{if } \frac{\mathrm{d}L_0}{\mathrm{d}t} \leq 0 \end{cases} \tag{12.42}$$

$$T_w(L_0+L_1) = \begin{cases} T_{w2} & \text{if } \frac{\mathrm{d}L_1}{\mathrm{d}t} > 0 \\ T_{w2} & \text{if } \frac{\mathrm{d}L_1}{\mathrm{d}t} \leq 0 \end{cases} \tag{12.43}$$

The mass and energy balance equations for the working fluid flowing through the evaporator tube in the three flow regimes of interest are written as follows,

Subcooled zone:

$$\begin{aligned} \textbf{\textit{Mass}}: \quad & A(\rho_0 - \rho')\frac{\mathrm{d}L_0}{\mathrm{d}t} + AL_0\left(\left.\frac{\mathrm{d}\rho_0}{\mathrm{d}P}\right|_h + \frac{1}{2}\left.\frac{\mathrm{d}\rho_0}{\mathrm{d}h}\right|_P\frac{\mathrm{d}h'}{\mathrm{d}P}\right)\frac{\mathrm{d}P_0}{\mathrm{d}t} \\ & + \frac{1}{2}AL_0\left.\frac{\mathrm{d}\rho_0}{\mathrm{d}h}\right|_P\frac{\mathrm{d}h_{\text{in}}}{\mathrm{d}t} = \dot{m}_{\text{in}} - \dot{m}_1 \end{aligned} \tag{12.44}$$

$$\begin{aligned} \textbf{\textit{Fluid energy}}: \quad & \frac{1}{2}A(\rho_0(h_{\text{in}} - h') - 2\rho' h' - 2P_0 + 2P(L_0))\frac{\mathrm{d}L_0}{\mathrm{d}t} \\ & + \frac{1}{2}AL_0\left(\rho_0 + \frac{1}{2}(h_{\text{in}} + h')\left.\frac{\mathrm{d}\rho_0}{\mathrm{d}h}\right|_P\right)\frac{\mathrm{d}h_{\text{in}}}{\mathrm{d}t} \\ & + \frac{1}{2}AL_0\left(\rho_0\frac{\mathrm{d}h'}{\mathrm{d}P} + (h_{\text{in}} + h')\left(\left.\frac{\mathrm{d}\rho_0}{\mathrm{d}h}\right|_P + \frac{1}{2}\left.\frac{\mathrm{d}\rho_0}{\mathrm{d}h}\right|_P\frac{\mathrm{d}h'}{\mathrm{d}P} - 2\right)\right)\frac{\mathrm{d}P_0}{\mathrm{d}t} \\ & = \dot{m}_{\text{in}}h_{\text{in}} - \dot{m}_1 h' + \pi D_i L_0 \alpha_{i0}(T_{w0} - T_o) \end{aligned} \tag{12.45}$$

$$\begin{aligned}\textbf{\textit{Tube energy}}:\quad & A_w\rho_w c_{p,w}\left(L_0\frac{dT_{w0}}{dt}+(T_{w0}-T_w(L_0))\frac{dL_0}{dt}\right)\\ &=\pi D_i L_0\alpha_{i0}(T_o-T_{w0})+q_0''L_0\end{aligned}\tag{12.46}$$

Two-phase zone:

$$\begin{aligned}\textbf{\textit{Mass}}:\quad & A(\rho'-\rho'')\frac{dL_0}{dt}+A(\rho'-\rho'')(1-\bar{\gamma})\frac{dL_1}{dt}\\ &+AL_1\left(\bar{\gamma}\frac{d\rho''}{dP}+(1-\bar{\gamma})\frac{d\rho'}{dP}\right)\frac{dP_1}{dt}=\dot{m}_1-\dot{m}_2\end{aligned}\tag{12.47}$$

$$\begin{aligned}\textbf{\textit{Fluid energy}}:\quad & A(\rho''h'-\rho''h''-P(L_0)+P(L_0+L_1))\frac{dL_0}{dt}\\ &+A((1-\bar{\gamma})(\rho'h'-\rho''h'')-P_1+P(L_0+L_1))\frac{dL_1}{dt}\\ &+AL_1\left(\bar{\gamma}\frac{d(\rho''h'')}{dP}+(1-\bar{\gamma})\frac{d(\rho'h')}{dP}-1\right)\frac{dP_1}{dt}\\ &=\dot{m}_1h'-\dot{m}_2h''+\pi D_iL_1\alpha_{i1}(T_{w1}-T_1)\end{aligned}\tag{12.48}$$

$$\begin{aligned}\textbf{\textit{Tube energy}}:\quad & A_w\rho_w c_{p,w}\begin{pmatrix}L_1\frac{dT_{w1}}{dt}+(T_w(L_0)-T_{w1})\frac{dL_0}{dt}\\ +(T_{w1}-T_w(L_0+L_1))\frac{dL_1}{dt}\end{pmatrix}\\ &=\pi D_iL_1\alpha_{i1}(T_1-T_{w1})+q_1''L_1\end{aligned}\tag{12.49}$$

Superheated zone:

$$\begin{aligned}\textbf{\textit{Mass}}:\quad & A(\rho''-\rho_2)\frac{dL_0}{dt}+A(\rho''-\rho_2)\frac{dL_1}{dt}\\ &+AL_2\left(\frac{1}{2}\frac{d\rho_2}{dP}\bigg|_P\frac{dh''}{dP}+\frac{d\rho_2}{dP}\bigg|_h\right)\frac{dP_2}{dt}\\ &+\frac{1}{2}AL_2\frac{d\rho_2}{dP}\bigg|_P\frac{dh_{\text{out}}}{dt}=\dot{m}_2-\dot{m}_{\text{out}}\end{aligned}\tag{12.50}$$

$$\begin{aligned}\textbf{\textit{Fluid energy}}:\quad & A\left(\rho''h''-\frac{1}{2}\rho_2(h''+h_{\text{out}})+P_2-P(L_0+L_1)\right)\left(\frac{dL_0}{dt}+\frac{dL_1}{dt}\right)\\ &+\frac{1}{2}AL_2\left((h''+h_{\text{out}})\left(\frac{1}{2}\frac{d\rho_2}{dP}\bigg|_P\frac{dh''}{dP}+\frac{d\rho_2}{dP}\bigg|_h\right)+\rho_2\frac{dh''}{dP}-2\right)\frac{dP_2}{dt}\\ &+\frac{1}{2}AL_2\left(\rho_2+\frac{1}{2}\frac{d\rho_2}{dP}\bigg|_P(h''+h_{\text{out}})\right)\frac{dh_{\text{out}}}{dt}\\ &=\dot{m}_2h''-\dot{m}_{\text{out}}h_{\text{out}}+\pi D_iL_2\alpha_{i2}(T_{w2}-T_2)\end{aligned}\tag{12.51}$$

$$\begin{aligned}\textbf{\textit{Tube energy}}:\quad & A_w\rho_w c_{p,w}\bigg[L_2\frac{dT_{w2}}{dt}+(T_w(L_0)-T_{w1})\frac{dL_0}{dt}\\ &+(T_w(L_0+L_1)-T_{w2})\left(\frac{dL_0}{dt}+\frac{dL_1}{dt}\right)\bigg]\\ &=\pi D_iL_2\alpha_{i2}(T_2-T_{w2})+q_2''L_2\end{aligned}\tag{12.52}$$

All the symbols bear the same meaning as mentioned in ref. (Yebra et al. 2005). Computational investigations can be performed by using the above one-dimensional model (Eqs. 12.40–12.52) and by training the initial conditions according to the experimental findings available from the real-life solar thermal power plants, with a view to comparing the computational cost as well as the accuracy of numerical predictions with the aforementioned reduced order dynamic model.

The dynamic moving boundary model can be improved further by incorporating axial variation in the heat transfer fluid temperature profile in shell and tube heat exchanger and by introducing time-dependent fluctuations in the subcooled refrigerant flow at the heat exchanger entry. Study of the transient moving boundary characteristics for different steady-state mean pressure values and for different extent of the dynamic fluctuations will a facilitate a better understanding about the feasible operating conditions and will help in the instrumentation for the advanced control of the solar thermal load loop.

References

Aguilar C, White D, Ryan D (2005) Domestic water heating and water heater energy consumption in Canada. Canadian Building Energy End-Use Data and Analysis Centre (CBEEDAC), Edmonton, AB, Report 2005-RP-02

Baddou Y (2017) Solar thermal systems for domestic water heating applications in residential buildings. Efficiency and economic viability analysis of monitored plants. Master Thesis, UEMF-Morocco/UPC Barcelona-Spain

Bauer O (1999) Modelling of two-phase flows with Modelica™. Master Thesis, Department of Automatic Control, Lund Institute of Technology, ISSN 0280-5316, ISRN LUTFD2/TFRT-5639-SE

Beck BT, Wedekind GL (1981) A generalization of the system mean void fraction model for transient two-phase evaporating flows. J Heat Transfer 103:81–85

Becker B, Stogsdill K (1990) A domestic hot water use database. ASHRAE J, 21–25

Behar O, Khellaf A, Mohammedi K (2015) A novel parabolic trough solar collector model—validation with experimental data and comparison to Engineering Equation Solver (EES). Energy Convers Manag 106:268–281

Cruz JB, Muñoz LJY, Bencomo SD, Moya EZ (2013) Modeling and simulation of two-phase flow evaporators for parabolic-trough solar thermal power plants. Gobierno de España, Ministerio de economía y competitividad, ISBN: 978-84-7834-705-6, NIPO: 721-13-044-9, 268 pages

Davidson JH (2005) Low-temperature solar thermal systems: an untapped energy resource in the United States. J Sol Energy Eng 127(3):305–306

Desideri A, Dechesne B, Wronski J, van den Broek M, Gusev S, Lemort V, Quoilin S (2016) Comparison of moving boundary and finite-volume heat exchanger models in the modelica language. Energies 9(5):1–18

Dittus FW, Boelter LMK (1930) Heat transfer in automobile radiators of the tubular type. Univ Calif Publ Eng 2:443–461

Donowski VD, Kandlikar SG (1999) Correlating evaporation heat transfer coefficient of refrigerant R-134a in a plate heat exchanger. Mechanical Engineering Department, Rochester Institute of Technology, Rochester, NY

Du P, Xu Y-F, Li M-L, Cai Z-H (1996) The transient characteristics of parallel flow plate-fin heat exchangers, energy and environment. In: Proceedings of the international conference on energy and environment, ICEE 1996, Begell House Inc, New York, pp 442–447

Eldredge BD, Alleyne AG (2006) Improving the accuracy and scope of control-oriented vapor compression cycle system models. ACRC TR-246, Air Conditioning and Refrigeration Center, University of Illinois Mechanical and Industrial Engineering Department

Endalew A, Abebe K (2012) Numerical modelling and experimental validation of heat tube solar collector for water heating. Master of Science Thesis, Energy Technology, Division of Thermodynamics and Refrigeration

Evarts JC, Swan LG (2013) Domestic hot water consumption estimates for solar thermal system sizing. Energy Build 58:58–65

Fairey P, Parker D (2004) A review of hot water draw profiles used in performance analysis of residential domestic hot water systems. Florida Solar Energy Center/University of Central Florida, Cocoa, FL, Report FSEC-RR-56-04, 20 July 2004

Gnielinski V (1975) Neue Gleichungen für den Wärme- und den Stoffübergang in turbulent durchströmten Rohren und Kanälen. Forschung im Ingenieurwesen (Engineering Research) 41:8–16

Grald EW, MacArthur JW (1992) A moving boundary formulation for modeling time-dependent two-phase flow. Int J Heat Fluid Flow 13:266–272

Heat Exchangers for Solar Water Heating Systems (2018) Available from: https://www.energy.gov/energysaver/heat-exchangers-solar-water-heating-systems. Accessed April 2018

Hobson PA, Norton B (1988) Verified accurate performance simulation model of direct thermosyphon solar energy water heaters. J SolEnergy Eng 110:282–292

Hoevenaars EJ, Crawford CA (2012) Implications of temporal resolution for modelling renewables-based power systems. Renew Energy 41:285–293

Homola CA (2018) Solar domestic hot water heating systems design, installation and maintenance. http://www.asse-plumbing.org/chapters/NOH%20SolarWtrHtg%20Pres.pdf. Accessed April 2018

IRC Online Fluid Property Calculator (2018) https://www.irc.wisc.edu/properties/. Accessed 15 May 2018

Isobaric Properties for Ethane, 1,1,1,2-tetrafluoro- (R134a), NIST Chemistry WebBook, SRD 69, National Institute of Standards and Technology, U.S. Department of Commerce. Accessed 15 May 2018

Jensen JM, Tummescheit H (2002) Moving boundary models for dynamic simulations of two-phase flows. In: Otter M (ed) Proceedings of the 2nd international Modelica conference, Oberpfaffhenhofen, Germany, pp 235–244

Kakaç S, Bergles AE, Fernandes EO (eds) (1988) Two-phase flow heat exchangers, thermal-hydraulic fundamentals and design. NATO ASI Series book series (NSSE), vol 143, Springer, Dordrecht, Print ISBN: 978-94-010-7755-2

Kalogirou S (2009) Thermal performance, economic and environmental life cycle analysis of thermosiphon solar water heaters. Sol Energy 83(1):39–48

Kalogirou SA, Tripanagnostopoulos Y (2006) Hybrid PV/T solar systems for domestic hot water and electricity production. Energy Convers Manag 47:3368–3382

Khan TS, Khan MS, Chyu M-C, Ayub ZH (2010) Experimental investigation of single phase convective heat transfer coefficient in a corrugated plate heat exchanger for multiple plate configurations. Appl Thermal Eng 30:1058–1065

Kim MB, Park CY (2017) An experimental study on single phase convection heat transfer and pressure drop in two brazed plate heat exchangers with different chevron shapes and hydraulic diameters. J Mech Sci Technol 31(5):2559–2571

Koffi PME, Andoh HY, Gbaha P, Touré S, Ado G (2008) Theoretical and experimental study of solar water heater with internal exchanger using thermosiphon system. Energy Convers Manag 49:2279–2290

Lakhani S, Raul A, Saha SK (2017) Dynamic modelling of ORC-based solar thermal power plant integrated with multitube shell and tube latent heat thermal storage system. Appl Therm Eng 123:458–470

Li W, Hrnjak P (2016) Single phase pressure drop and flow distribution in brazed plate heat exchangers. In: 16th international refrigeration and air conditioning conference at Purdue, 11–14 July 2016

Li H, Hrnjak P (2017) Measurement of heat transfer coefficient and pressure drop during evaporation of R134a in new type facility with one pass flow through microchannel tube. Int J Heat Mass Transf 115:502–512

Lunde PJ (1980) Solar thermal engineering: space heating and hot water systems. OSTI ID: 5819885, Unites States

Majumdar R, Saha SK (2018) Quasi-steady state reduced order moving boundary model of ORC heat exchanger for medium temperature solar-thermal systems. In: Proceedings of the international conference on sustainable energy and environmental challenges (SEEC-2018), IISc. Bangalore, India, 01–03 Jan 2018

Majumdar R, Singh S, Saha SK (2018a) Quasi-steady state moving boundary reduced order model of two-phase flow for ORC refrigerant in solar-thermal heat exchanger. Renew Energy 126:830–843

Majumdar R, Saha SK, Singh S (2018b) Evaluation of transient characteristics of medium temperature solar thermal systems utilizing thermal stratification. Appl Energy 224:69–85. https://doi.org/10.1016/j.apenergy.2018.04.083

Manglik RM (2006) On the advancements in boiling, two-phase flow heat transfer, and interfacial phenomena. J Heat Transfer 128(12):1237–1242

Mani A, Rangarajan S (1982) Solar radiation over India. Allied Publishers Private Limited, New Delhi, 647 pages

Mathioulakis E, Belessiotis V (2002) A new heat-pipe type solar domestic hot water system. Sol Energy 72(1):13–20

Mehendale SS (2017) Single-phase heat exchangers. In: Kulacki F (eds) Handbook of thermal science and engineering. Springer, Cham, Online ISBN: 978-3-319-32003-8

Meyer M (2014) Heat transfer and pressure drop in the condensing superheated region with visualization and film thickness measurement. M.S. Thesis, University of Illinois at Urbana-Champaign

Mills D (2004) Advances in solar thermal electricity technology. Sol Energy 76:19–31

MNRE Annual Report: 2006–2007 (2007) Ministry of New and Renewable Energy (MNRE). Government of India, CGO Complex, Lodhi Road, New Delhi

Mongibello L, Bianco N, Di Somma M, Graditi G, Naso V (2014) Numerical simulation of a solar domestic hot water system. In: 32nd UIT (Italian Union of Thermo-fluid-dynamics) heat transfer conference, Journal of Physics: Conference Series, 547

Muley A, Manglik RM (1997) Enhanced heat transfer characteristics of single-phase flows in a plate heat exchanger with mixed Chevron plates. J Enhanced Heat Transf 4(3):187–201. https://doi.org/10.1615/JEnhHeatTransf.v4.i3.30

Natural Resources Canada (NRCan): Survey of household energy use—summary report (December 2005). http://oee.nrcan.gc.ca/Publications/statistics/sheu-summary/pdf/sheu-summary.pdf. Accessed April 2018

Nilpueng K, Wongwises S (2015) Experimental study of single-phase heat transfer and pressure drop inside a plate heat exchanger with a rough surface. Exp Thermal Fluid Sci 68:268–275

Paynter HM, Takahashi Y (1956) A new method of evaluating dynamic response of counter flow and parallel flow heat exchangers. Trans ASME 78:749–758

Pinel P, Cruickshank CA, Beausoleil-Morrison I, Wills A (2011) A review of available methods for seasonal storage of solar thermal energy in residential applications. Renew Sustain Energy Rev 15(7):3341–3359

Pingaud H, Le Lann JM, Koehret B (1989) Steady-state and dynamic simulation of plate fin heat exchangers. Comput Chem Eng 13:577–585

Powell KM, Edgar TF (2012) Modeling and control of a solar thermal power plant with thermal energy storage. Chem Eng Sci 71:138–145

Renewable Energy Solutions, Solar Thermal- Domestic Hot Water Systems (DHWS) (2018) Available from: http://cf.cdn.unwto.org/sites/all/files/docpdf/re28solarthermal-domestichotwatersystemsdhwsfaq.pdf. Accessed April 2018

Roetzel W (1996) Transient analysis in heat exchangers. In: Afgan N et al (eds) New developments in heat exchangers. Gordon and Breach Publishers, Amsterdam, pp 547–575

Roetzel W, Xuan Y (1999) Dynamic behaviour of heat exchangers. In: International series on developments in heat transfer. WIT Press, Boston, 380 pages

Sarbu I, Adam M (2011) Applications of solar energy for domestic hot–water and buildings heating/cooling. Int J Energy 5(2):34–42

Shi R, He T, Peng J, Zhang Y, Zhuge W (2016) System design and control for waste heat recovery of automotive engines based on organic Rankine cycle. Energy 102:276–286

Shinde A, Sankalp A, Pramod KM, Rao PVC, Saha SK (2017) Heat transfer characterization and optimization of latent heat thermal storage system using fins for medium temperature solar applications. J Sol Energy Eng ASME 139:031003-(1-10)

Shoureshi R, McLaughlin K (1984) Modeling and dynamics of two-phase flow heat exchangers using temperature—entropy bond graphs. In: Proceedings of American control conference, San Diego, CA, USA, pp 93–98

Single Phase Fluid Coils (2018) Available from: http://www.srcoils.com/2887wp/wp-content/uploads/2012/06/CW-Coil-Primer.pdf. Accessed April 2018

Solar Thermal Hot Water Systems and Individual Components (2018) STIEBEL ELTRON, http://www.stiebel-eltron-usa.com/products/solar-thermal-hot-water-systems-individual-components. Accessed April 2018]

Sung T, Yun E, Kim HD, Yoon SY, Choi BS, Kim K, Kim J, Jung YB, Kim KC (2016) Performance characteristics of a 200-kW organic Rankine cycle system in a steel processing plant. Appl Energy 183:623–635

Taherian H, Rezania A, Sadeghi S, Ganji DD (2011) Experimental validation of dynamic simulation of the flat plate collector in a closed thermosyphon solar water heater. Energy Convers Manag 52:301–307

Tang R, Cheng Y, Wu M, Li Z, Yu Y (2010) Experimental and modeling studies on thermosiphon domestic solar water heaters with flat-plate collectors at clear nights. Energy Convers Manag 51:2548–2556

Tchuen G, Koholé WY (2017) A numerical investigation of three different thermosyphon solar water heating systems. Int J Ambient Energy, 1–12

Thirugnanasambandam M, Iniyan S, Goic R (2010) A review of solar thermal technologies. Renew Sustain Energy Rev 14(1):312–322

Thome JR (1990) Enhanced boiling heat transfer, Hemisphere, New York, 356 pages

Todreas NE, Kazimi MS (1993) Nuclear systems I, Thermal hydraulic fundamentals. Taylor and Francis, Abingdon

Vélez F, Chejne F, Quijano A (2014) Thermodynamic analysis of R134a in an Organic Rankine cycle for power generation from low temperature sources. DYNA 81:153–159

Voller V, Cross M (1981) Accurate solutions of moving boundary problems using the enthalpy method. Int J Heat Mass Transfer 24:545–556

Wedekind GL, Bhatt BL, Beck BT (1978) A system mean void fraction model for predicting various transient phenomena associated with two-phase evaporating and condensing flows. Int J Multiphase Flow 4:97–114

Weiss W (ed) (2012) Solar heating systems for houses: a design handbook for solar combisystems. Routledge (an imprint of the Taylor & Francis Group), ISBN 1 902916468, 330 pages

Wood AS (1991) A note on the use of the isotherm migration method. J Comput Appl Math 36:371–384

Wormley DN, Masada GY (1982) Evaluation of lumped parameter heat exchanger dynamic models. ASME Paper 82-WA/DSC-16

Yebra LJ (2006) Modelado orientado a objetos con Modelica de plantas de energía solar basadas en colectores cilindro-parabólicos. Ph.D. Thesis, Universidad Nacional de Educación a Distancia (UNED), Madrid, Spain

Yebra LJ, Berenguel M, Dormido S (2005) Extended moving boundary model for two-phase flows. IFAC Proc Volumes 38(1):368–373

Zelzouli K, Guizani A, Kerkeni C (2014) Numerical and experimental investigation of thermosyphon solar water heater. Energy Convers Manag 78:913–922

Zhang W-J, Zhang C-L (2006) A generalized moving boundary model for transient simulation of dry expansion evaporators under larger disturbances. Int J Refrig 29:1119–1127